Redox heterogeneities in a subducting slab: Example from the Monviso meta-ophiolite (Western Alps, Italy)

C. Caurant, Baptiste Debret, B. Ménez, C. Nicollet, P. Bouilhol

Redox heterogeneities in a subducting slab: example from the Monviso meta-ophiolite (Western Alps, Italy)

C. Caurant[1], B. Debret[1]*, B. Ménez[1], C. Nicollet[2] and P. Bouilhol[3]

[1]Université Paris Cité, Institut de physique du globe de Paris, CNRS, Paris, France.

[2]Laboratoire Magmas et Volcans, Université Clermont Auvergne, CNRS, IRD, OPGC, Clermont-Ferrand, France.

[3]Université de Lorraine, CNRS, CRPG, Nancy, France.

*corresponding author: Baptiste Debret (debret@ipgp.fr)

Highlights

- Heterogeneous oxygen fugacity recorded in serpentinites of the Monviso meta-ophiolite
- Subducting slab redox gradient set up during serpentinite dehydration at eclogite facies P-T conditions
- Carbonaceous matter precipitation enhanced by carbonate reduction in the slab

Abstract

Variations of redox conditions (i.e., oxygen fugacity, fO_2) accompanying slab dehydration in subduction zones are subject to ongoing controversies, especially since the interplay between redox sensitive elements during prograde metamorphism remains complex and, likely, variable at the slab scale. Here we investigate fO_2 variations during serpentinite dehydration and their feedback on the stability of sulfur and carbon compounds by studying the eclogitic Monviso meta-ophiolite (Western Alps, Italy). Despite a complex metamorphic history, the Monviso massif has preserved a complete section of oceanic lithosphere, from seafloor metasediments, meta-ophicarbonates and metabasites to deep-seated metagabbros and metaserpentinites. By bringing new estimates in the northern massif, we show that these lithologies have recorded a homogeneous pressure and temperature (P-T) climax, at 520-570°C and 2.6-2.7 GPa, on the whole meta-ophiolite. Despite this homogeneous P-T record, serpentinite forming minerals imply strong variations in fO_2 according to their position in the slab, from high fO_2 conditions (~ FMQ +2) in the deep-seated lithologies made of heazlewoodite-magnetite-olivine assemblages to low fO_2 (~ FMQ -4) in the paleoseafloor lithologies made of pentlandite-awaruite-olivine. This redox gradient is opposed to what is expected at mid-ocean ridges and is

29 therefore likely set up during serpentinite dehydration. Such variations of fO_2 conditions also
30 influenced carbon distribution and redox state within the lithosphere. In particular, reducing
31 conditions associated with brucite breakdown in paleoseafloor serpentinites promote the formation
32 of disordered carbonaceous matter over inorganic carbonates. Newly-formed disordered
33 carbonaceous matter could subsequently be recycled in the deep mantle, with the potential to play a
34 major role on the deep carbon cycle.

35 # 1. Introduction

36 Fluid/rock interactions between the slab and the mantle wedge are central in understanding
37 geochemical cycles in subduction zones. These are particularly sensitive to redox processes and oxygen
38 fugacity (fO_2) that govern both element speciation in fluids and mineral equilibria at high pressure and
39 high temperature (HP-HT). Strong redox gradients are observed in HP-HT slab relicts in mountain
40 ranges (meta-ophiolites) and in active or orogenic mantle wedge areas (e.g., Tumiati & Malaspina,
41 2019). Although the latter were clearly shaped during subduction by slab-derived fluid percolation,
42 ongoing controversies concern the origin of redox variations in meta-ophiolites and whether or not
43 these are inherited from an abyssal stage (e.g., Bretscher et al., 2018; Vieira Duarte et al., 2021) or
44 settled during prograde metamorphism (Debret et al., 2015; Padrón-Navarta et al., 2021).
45 Serpentinites have the potential to record redox evolution within the subduction system. These rocks
46 are observed in both slab and mantle wedge relicts, and have preserved a high level of redox
47 heterogeneities (i.e., strong variations in fO_2), with samples equilibrated between -4 to +3 relative to
48 Fayalite-Magnetite-Quartz buffer (FMQ; Debret et al., 2015; Debret & Sverjensky, 2017; Evans et al.,
49 2017; Evans & Frost, 2021; Evans & Powell, 2015; Galvez et al., 2013; Piccoli et al., 2019; Vitale
50 Brovarone et al., 2017). For example, the observation of graphite-like horizons at the contact between
51 metaserpentinites and metasedimentary rocks in slab related Alpine meta-ophiolites (Galvez et al.,
52 2013; Vitale Brovarone et al., 2017) suggests that fluid/rock interactions can promote carbonate
53 reduction into methane and/or graphitic material constraining the assemblage observed in

metaserpentinites to FMQ -4. At the opposite, highly oxidizing conditions were recorded in chlorite-harzburgites formed during antigorite breakdown in the Cerro del Almirez massif (Spain; Debret et al., 2015). There, the formation of hemo-ilmenite, chlorite, olivine and orthopyroxene could have been equilibrated up to FMQ +3. To complement these observations, thermodynamic and experimental studies have recently investigated fO_2 variations during serpentinite dehydration and highlighted the role of protolith (i.e., abyssal serpentinite) composition and mineralogy influencing metamorphic reactional pathways during subduction (Debret & Sverjensky, 2017; Evans et al., 2017; Evans & Frost, 2021; Evans & Powell, 2015; Iacovino et al., 2020; Lazar, 2020; Maurice et al., 2020; Vieira Duarte et al., 2021). However, when extrapolated to subduction systems, these models must be taken with caution as they often compare fO_2 retrieved from bulk compositions and phase assemblages from various geological settings, with sometimes large uncertainties regarding the geodynamical setting (e.g., Cerro del Almirez, Spain).

The Western Alps are a relevant natural laboratory to study the oceanic lithosphere cycle in subduction zones. They are among the best subduction archives in the world, with abundant eclogitic meta-ophiolites (500-650°C, 2.0-2.5 GPa) preserving fragments of oceanic mantle peridotites, gabbros, thinned continental margin and pelagic sediments partly within their pre-collisional architecture (Agard, 2021; Bernouilli et al., 2003). Subducted fragments experienced conditions typical of mature subduction worldwide before exhumation and juxtaposition during Alpine orogeny. Here we investigate the redox variations recorded in ultramafic rocks (i.e., not only metaserpentinites but also meta-ophicarbonates and chloriteschists) composing the Monviso meta-ophiolite (Italy). This meta-ophiolite is a well-characterized section of oceanic lithosphere (Angiboust et al., 2012; Balestro et al., 2011, 2013; Locatelli, Federico, et al., 2019; Lombardo et al., 1978) that was subducted to eclogite facies P-T conditions before being exhumed during the Alpine orogeny. Based on thermodynamic models and petrological observations, we show that the meta-ophiolite recorded strong redox heterogeneities at eclogite facies conditions, from basal serpentinites equilibrated at about FMQ +2 as opposed to paleoseafloor serpentinites equilibrated at about FMQ -4. This redox gradient is opposed

to what is expected at mid-ocean ridges in modern settings suggesting that it was settled during subduction. Interestingly, reducing conditions associated with paleoseafloor lithologies are likely promoted by carbonate reduction into disordered carbonaceous matter.

2. Geological setting

The Monviso meta-ophiolite is a mafic/ultramafic unit extending over 30 km along strike at the French–Italian border (Figure 1). It belongs to the Ligure Piemontese domain of the Western Alps, which regroups fragments of the Tethys oceanic lithosphere later subducted with the European continental crust under the Apulian margin, and exhumed during the Alpine orogeny (see review by Agard, 2021). The Monviso meta-ophiolite is separated from the blueschist-facies Queyras Schistes Lustrés Complex to the West and from the eclogite-facies Dora Maira continental unit to the East by two ductile normal faults (Ballèvre et al., 1990; Blake & Jayko, 1990). The first modern geological map of the southern part of the Monviso massif was made by Lombardo et al. (1978) and was completed by Balestro et al. (2013) and Locatelli, Federico, et al. (2019). The northern part of the massif was more recently mapped by Balestro et al. (2011).

The Monviso massif is mainly made of calcschists, pillowlavas, metabasalts, metagabbros and metaserpentinites. The original lithostratigraphical subdivision of the Monviso meta-ophiolite was defined in the southern part of the massif by Lombardo et al. (1978). These authors distinguished six N-S striking and W-dipping subunits disrupted by shear zones, namely, from East to West, the Basal Serpentinite Unit, the Lago Superiore Unit, the Viso Mozzo Unit, the Passo Gallarino Unit, the Costa Ticino Unit, and the Vallanta metabasite Unit. This division was supported by P-T estimates on metagabbros, whereby ad hoc thermo-barometers (Ellis & Green, 1979; Pattison & Newton, 1989) showed a heterogeneous metamorphic record along the massif, ranging from 450 ± 40°C - 1.2 ± 0.3 GPa in the Passo Gallarino Unit to 620 ± 50°C - > 2.4 GPa in the Lago Superiore Unit (Blake et al., 1995; Schwartz et al., 2001). However, this model was revised by Angiboust et al. (2012) who tested potential heterogeneities within and between the various subunits using thermodynamic models applied to

metagabbros and Raman Spectroscopy of Carbonaceous Material (RSCM) thermometry in metasedimentary rocks. These new P-T estimates rather suggest the existence of two main coherent tectonometamorphic subunits expending over 20 km long, namely the Upper and Lower Tectonic Units (also named Monviso and Lago superior Units in Angiboust et al., 2012; Figure 1). Each tectonometamorphic subunits has recorded a difference in temperature of about 70°C, with the Upper Tectonic Units being equilibrated at 480°C-2.2 GPa and the Lower Tectonic Units recording a metamorphic climax at 550°C-2.6 GPa. They were then juxtaposed at epidote–blueschist facies during Alpine orogeny and are now separated by an Alpine-related West-dipping shear zone, namely the Upper Shear Zone (USZ) (Figure 1a; Angiboust et al., 2012). More recently, Balestro et al. (2018) and Festa et al. (2015) proposed that the Lower Tectonic Unit could have been derived from an oceanic core complex, with some major shear zones resulting from the reactivation of pre-Alpine structures (e.g., oceanic detachment fault, ODF). These structures were evidenced in the northern part of the massif where the contact between metasedimentary rocks and (ultra)mafic units has been interpreted as a paleo-ODF (Figure 1a-c) separating seafloor (ophicarbonates, basalts and sedimentary rocks) and deep-seated (serpentinites and gabbros) oceanic lithologies. In the southern part of the Lower Tectonic Unit, metasedimentary units are quasi-absent and the continuation of these paleoseafloor structures remains unclear (Figure 1a). Indeed, these were intensively reworked and overprinted by Alpine-related shear zones, namely the Intermediate and Lower Shear Zones (ISZ and LSZ, respectively; Figure 1d-e; Angiboust et al., 2012, 2014). It is interesting to note that, despite numerous studies focusing on the Monviso meta-ophiolite over the last 30 years, the lack of systematic P-T estimates on the northern part of the massif does not allow a truthful comparison of the metamorphic record from North to South in the massif.

3. Field occurrence of the studied samples

Our study aims at comparing the metamorphic and redox record of ultramafic rocks (metaserpentinites, meta-ophicarbonates, chloriteschists) along the Monviso Lower Tectonic Unit. The

studied rocks were sampled along four cross sections (Figure 1b-e), namely from North to South, Colle del Baracun, Colle Armoine, Lago Superiore/Lago Fiorenza and Rifugio Quintino Sella cross sections. In addition, few metasedimentary rocks were sampled at the contact with ultramafic rocks for RSCM thermometry purpose.

3.1 Northern massif sampling

Both Colle del Baracun and Colle Armoine cross sections are characterized by a high amount of metasedimentary rocks stratigraphically sitting on metaserpentinites (thereafter referred to as paleoseafloor serpentinites, Figure 1b-c). The Colle del Baracun cross section represents an overturned fold, with the core of the fold consisting of paleoseafloor lithologies including metasedimentary rocks and few metabasalts overlying metaserpentinites (Figure 1b). Toward to the East, the limbs of the fold are composed of a ~ 300 m thick metaserpentinite layer made of foliated serpentinites embedding metagabbroic pods of several metres in length. This deep-seated sequence is referred to as a basal serpentinite layer, outcropping from North to South (Lombardo et al., 1978) and stratigraphically sitting below the paleoseafloor lithologies. The Colle Armoine cross section is characterized by a recumbent geometry with the core of the synformal anticlines consisting of metaserpentinites, and the limbs of metasedimentary rocks (Figure 1c). To the East, these paleoseafloor lithologies are separated from basal serpentinites by the LSZ.

Paleoseafloor lithologies were sampled at the Colle del Baracun and the Colle Armoine sensus stricto (Figure 1a). In these areas, the contacts between metasedimentary rocks and metaserpentinites are marked by intensively sheared metasomatic chloriteschist layers of several metres in length. The chloriteschists are highly foliated and can display diopside and/or tremolite layers of several centimetres thickness, associated with numerous magnetite crystals of millimetre size (Figure 2a). Massive centimetric to metric blocks of lawsonite-rich eclogites and meta-ophimagnesites (Figure 2b) are embedded within chloriteschist foliation in both localities. Below the metasomatic shear zone, the paleoseafloor serpentinites can be associated with a pervasive network of brown veins mainly made of olivine, sometimes associated with centimetric titanoclinohumite crystals (Figure 2c).

Basal serpentinites were collected nearby the Rifugio Barbara Lowrie and toward to the North nearby Villanova village (Figure 1a-b). At Rifugio Barbara Lowrie, metaserpentinites were sampled along a cliff made of an alternance of metric to centimetric brown olivine-rich and dark blue serpentine-rich layers (Figure 2d). The brown layers form a dense anastomosed network of veins that cross-cut the dark-blue host serpentinite. Meta-rodingite dykes are also observed along the cliff. They display a black chlorite wall of about 10 cm in width, mainly made of chlorite, diopside, magnetite and andradite in contact with the host serpentinites. The Villanova metaserpentinites are intensively sheared and finely recrystallized. The rock foliation is materialised by small brown planes of several millimetre in width with sigmoidal shapes mainly made of olivine. The rock foliation can embed decimetre to metre sized boudins of massive serpentinite with a pale green colour.

3.2 Southern massif sampling

The Lago Superiore/Lago Fiorenza and Rifugio Quintino Sella cross sections display similar lithostratigraphic structures. They consist, from West to East, of metabasalts structurally overlying a thick sequence of metagabbros and metaserpentinites (Figure 1d-e). Relative to those of the northern part of the massif, these cross sections are characterized by scarce metasedimentary rocks and a large amount of metabasites. To the East, the cross sections are cut by the LSZ that separates metabasites from basal serpentinites (Angiboust et al., 2012; Locatelli, Verlaguet, et al., 2019). The LSZ includes highly deformed meta-ophidolomites within a serpentinite matrix (thereafter named LSZ-serpentinites). The LSZ-serpentinites are highly foliated and can embed massive serpentinite blocks of several metres in width. They are composed of an alternance of antigorite-rich and olivine-rich layers with sigmoidal shapes that contribute to a S-C fabric (Figure 2e – see also Schwartz et al., 2013). To the West, the USZ (Figure 1a) also includes large block of meta-ophidolomites of metric size. Metasedimentary rocks, meta-ophidolomites and LSZ-serpentinites were sampled at the Lago Superiore/Lago Fiorenza and nearby the Rifugio Quintino Sella. Beyond the LSZ to the East, the basal serpentinites are variably foliated with a West-dipping foliation and includes metre sized eclogitic

lenses. This unit was not resampled as sufficient data are already provided in the literature for this specific area (Gilio et al., 2020; Schwartz et al., 2013).

4. Methods

4.1 Bulk rock analyses

Bulk rock major and volatile (carbon and sulfur) elements were analysed at the SARM (Service d'Analyses des Roches et des Minéraux, Nancy, France) by Inductively Coupled Plasma Optical Emission Spectrometry (Thermo Scientific iCAP 6500) and HORIBA EMIA-320V2 Carbon/Sulfur Analyser, respectively. Sample digestions for major elements (SiO_2, Al_2O_3, Fe_2O_3, MnO, MgO, CaO, Na_2O, K_2O, TiO_2) were performed using $LiBO_2$ flux fusion process following the procedure described by Carignan et al. (2001). The analyses were accurate within 1–5% for SiO_2, Al_2O_3, Fe_2O_3, MnO, MgO, CaO, Na_2O, K_2O and within 1–10% for TiO_2 based on repeated analyses of U.S. Geological Survey and CRPG standards (Carignan et al., 2001).

4.2 Silicate and sulfide in situ analyses

In situ major element concentrations of the rock forming minerals were obtained in punctual mode on C-coated petrographic thin sections using a CAMECA SXFive electron microprobe at the CAMPARIS platform, Sorbonne Université (Paris, France; accelerating voltage 15 kV, beam current 10 nA). For representative analyses of major mineral phases, the reader is referred to Supplementary Table S1. Scanning Electron Microscope (SEM) observations were performed at the platform PARI of the Institut de physique du globe de Paris of Université Paris Cité (IPGP-UPC, France) using a Zeiss EVO MA-10 and a Zeiss Auriga FEG-FIB on Au-coated petrographic thin sections. Images were collected using a backscattered electron (BSE) detector (NTS BSD) at 15 kV accelerating voltage and high current. Energy dispersive X-ray spectrometry (EDS) measurements were performed using a Bruker Quantax 200 detector (125 eV resolution).

4.3 Carbonaceous compound characterization

Sample preparation for in situ carbon compound characterization was performed at IPGP-UP. Rock samples were sawed with a cleaned Cu-core diamond blade and sterile ultrapure water to extract the

inner core, free of possible post-sampling organic contamination. The inner core was then manipulated using clean pliers, thinned and polished on both faces (down to a thickness of tens of micrometres) with pure ethanol using alumina polishing disks without any use of resin or glue.

SEM observations were performed on Au-coated samples at the platform PARI of the IPGP-UP using a Zeiss Auriga 40 field emission scanning electron microscope. Backscattered electron images were collected at high current with accelerating voltage ranging from 10 kV to 15 kV, at respectively low and high currents (from 10 pA to 1 nA), using a NTS BSD detector. EDS maps were collected at 15 kV accelerating voltage using a Bruker Quantax 200 detector. Elemental distributions were processed using the ImageJ software (Schneider et al., 2012). False colour images were obtained using PhotoFiltre 7 software.

Raman spectroscopy was performed on resin-free samples at the platform PARI of the IPGP-UP with a Renishaw InVia spectrometer using the 514nm wavelength of a 20 mW argon laser focused through an Olympus BX61 microscope with a x50 objective (numerical aperture: 0.75). This configuration yields a planar resolution close to 1 µm. The laser power delivered at the sample surface was 0.5 mW with integration times of 150 s, well below the critical dose of radiation that can damage carbonaceous matter (Beyssac et al., 2003). Light was dispersed by a holographic grating with 1800 grooves mm^{-1} and the signal analysed with a RENCAM charge-coupled device detector. Acquisition times were set at 5 × 30s. Raman was used to identify and characterize both silicates (e.g., serpentine minerals) and carbonaceous matter and for RSCM thermometry. As the chemical and structural evolution of carbonaceous matter after a temperature increase is irreversible, RSCM thermometry is a convenient tool to estimate maximum temperature experienced by sedimentary organic matter in the range of 330-640 (± 50) °C. For each metasediment sample, 10 spectra were averaged to smooth out the within-sample structural heterogeneity. Spectra were then fitted using PeakFit software (Systat Software, Inc.), based on the method of Beyssac et al. (2002).

4.4 Thermodynamic models

We use a Gibbs free energy minimization strategy (Connolly, 2005, 2009) to compute, using Perplex software, phase equilibria in metaserpentinites during subduction. Pseudosections were calculated for four representative samples of paleoseafloor (VIS18-5A1 and VIS18-7 samples), LSZ- (VIS18-3 sample) and basal (VIS20-1 sample) serpentinites (Table 1 and Supplementary Table S2). These samples were selected as they host contrasted HP parageneses, made of antigorite-olivine (VIS18-3, VIS18-5A1 and VIS20-1 samples) or antigorite-chlorite-diopside/tremolite (VIS18-7 sample), and redox-sensitive accessory phases, made of awaruite-pentlandite (VIS18-3 and VIS18-5A1 sample) or heazlewoodite-magnetite (VIS20-1 sample). This sample set is considered as representative of the mineralogical variations observed in the metaserpentinites constituting the Monviso meta-ophiolite.

Phase diagrams in SiO_2-FeO-MgO-CaO-H_2O [CO_2-NiO-S_2-O_2] systems were calculated using the Holland & Powell 1998 (revised in Holland & Powell, 2003) thermodynamic database. Al_2O_3 was not considered as the main Al-bearing phase would be chlorite, stable in all the studied rocks, whatever the considered P-T conditions. Although Al_2O_3 contents can enlarge the stability field of antigorite to higher temperatures (Padrón-Navarta et al., 2013), these effects were considered negligible at the investigated temperatures, i.e., below temperatures of antigorite breakdown (620°C). This therefore does not affect the phase relationships, neither the dehydration reactions at the considered conditions. In calculations with Ni-S bearing species, awaruite, heazlewoodite, vaesite, millerite, pentlandite, pyrite and pyrrhotite have been implemented in the database (Supplementary Table S3). The thermodynamic data of these pure species have been compiled from Evans et al. (2017), Holland & Powell (1998) and Klein & Bach (2009) and were previously benchmarked by Evans et al. (2017). A-X relationships are from Holland & Powell (2003) for olivine (with the addition of a Ni-olivine species "fran"), clinopyroxene, orthopyroxene, and amphibole (tremolite and Fe-tremolite); from Padrón-Navarta et al. (2013) for antigorite; from Sack & Ghiorso (1991) for magnetite-magnesioferrite; from Franzolin et al. (2011) for carbonates, with an enthalpy of formation of -5.74 kJ mol^{-1} for ordered dolomite (Navrotsky & Capobianco, 1987), which is considered to be in good accordance with natural

examples (e.g., Scambelluri et al., 2016, Debret et al. 2018). The fluid considered (COH-fluid, see perplex.ethz.ch) uses a hybrid equation of state derived from Connolly & Cesare (1993) and includes H_2S and SO_2 species. Carbon-bearing species were not considered in the thermodynamic modelling as current thermodynamic knowledge of organic compounds at HP-HT is limited to methane (CH_4) and acetate (CH_3COO^-) in fluids (Sverjensky et al., 2014), while several recent natural or experimental studies have highlighted that the later these simple organic species are likely to decompose to solid carbonaceous compounds, for which no thermodynamic database is available (e.g., Szlachta et al., 2022).

Few adjustments of serpentinite bulk rock composition were performed depending on the considered solution models. Pseudosections were calculated considering FeO, therefore excluding Fe_2O_3 linked to magnetite according to Kempf et al. (2020), and CaO bounded to silicates (Supplementary Table S2). The amount of FeO was calculated considering a constant Fe^{3+}/Fe_{total} ratio of 0.4, coherent with previous estimates in the eclogitic Alpine meta-ophiolites (Debret et al., 2014), and a ratio of 0.66 for magnetite. This was with the exception of pseudosections calculated in SiO_2-FeO-MgO-CaO-H_2O-NiO-S_2-O_2 system that attempt to model Fe-bearing accessory phases (i.e., magnetite, sulfides) during thermodynamic calculations. The amount of CaO was calculated removing CaO bounds to carbonate, based on CO_2 concentrations measured in bulk rock. This was with the exception of pseudosections in SiO_2-FeO-MgO-CaO-H_2O-CO_2 in which carbonates were implemented during thermodynamic calculations – assuming that all carbon contained in the samples is inorganic.

5. Thin section observations and in situ analyses

The studied cross sections show from East to West a succession of deep-seated oceanic lithologies (basal serpentinites and metagabbros) to paleoseafloor lithologies (including calcschists, metabasalts, meta-ophicarbonates and paleoseafloor serpentinites; Figure 1). Here we describe the thin section petrography of metasedimentary and ultramafic rocks composing the massif from top to bottom: (i) metasedimentary rocks, (ii) the metasomatic contacts made of chloriteschists embedding blocks of

meta-ophimagnesites, (iii) paleoseafloor serpentinites, (iv) LSZ-serpentinites and associated meta-ophidolomites related to shear zones in the southern part of the massif and (v) basal serpentinites.

5.1 Metasedimentary rocks

Metasedimentary rocks were sampled all along the massif, at the contact with ultramafic rocks in the northern massif and within the USZ and LSZ in the southern massif (Table 1). These rocks are mainly made of calcite, quartz, white micas and graphite. Metasedimentary rocks from the northern massif were selected to perform RSCM thermometry (Beyssac et al., 2002). Few variations in Raman spectra are observed passing from one sample to another (Figure 3). The obtained spectra are characterized by a broad disordered band (D) of low intensity at 1355 cm^{-1} and a sharp and more intense graphite band (G) at 1578 cm^{-1}. Temperatures obtained through the deconvolution of the D and G bands are shown in Figure 1a. Considering the errors of 50°C associated with these estimates (Beyssac et al., 2002), these temperatures overlap, ranging from 519°C at the Colle del Baracun to 558°C at the Colle Armoine.

5.2 Metasomatic contacts

Metasomatic contacts made of chloriteschists embedding meta-ophimagnesites (Figure 2a-b) were sampled at the interface between metasedimentary and ultramafic units in the northern part of the massif. The chloriteschists present an alternance of diopside (Di2)-rich and chlorite-rich folded layers (Figure 2a). Diopside layers are widely associated with large crystals of tremolite, interstitial talc and sulfides of more than 50 µm in width and can contain rare calcite relicts in their centre (Figure 4a-b). Both diopside and chlorite crystals are orientated along rock foliation and are associated with abundant magnetite. Di2 grains of about 100 µm in width with a XMg value (= Mg/(Mg + Fe)) ranging from 0.89 to 0.96 have low Al_2O_3 and Cr_2O_3 (<0.2 weight%, wt%) contents relative to mantle clinopyroxene (Supplementary Table S1), supporting a metamorphic origin (Nozaka, 2010). Chlorite crystallized as orientated lamellae of 200 µm in length. They have Al_2O_3 contents of 13.0-14.6 wt% and XMg values of 0.90-0.92. Raman and SEM analyses highlight the presence of carbonaceous matter in both diopside- and chlorite-rich layers (Figure 4c). Carbonaceous matter consists of dense aggregates

of about 10 µm in width with a gel-like texture and enclosed within diopside or chlorite crystals (Figure 4c). Associated Raman spectra are characterized by a broad and relatively intense D band at 1369 cm^{-1} and a relatively sharper G band at 1591 cm^{-1} (Figure 3). Based on these spectra, these are named disordered carbonaceous matter (DCM) hereafter.

Meta-ophimagnesites are made of large magnesite crystals of up to 10 cm in width surrounded by white metamorphic coronas (Figure 2b). The latter includes large magnetite crystals, up to 1 cm in width, associated with finely recrystallized assemblages made of antigorite-chlorite and dolomite-tremolite/diopside ± chlorite ± talc (Figure 4d). Antigorites are systematically associated with chlorite in their centre. Antigorites are characterized by variable Al_2O_3 contents ranging from 0.1 to 2.3 wt% and XMg values ranging from 0.90 to 0.93 (Supplementary Table S1). Chlorites have higher Al_2O_3 contents of 12.0 to 15.1 wt% and XMg values ranging from 0.88 to 0.92. DCM was also observed in the recrystallized assemblages, as embedded in chlorite. The associated Raman spectra are similar to those observed in chloriteschists and are marked by two broad D and G bands at 1369 cm^{-1} and 1591 cm^{-1}, respectively (Figure 3).

5.3 Paleoseafloor serpentinites

Paleoseafloor serpentinites are observed directly below the metasomatic contacts separating metasedimentary and ultramafic units. These rocks present highly variable amount of olivine or diopside either at sample or thin section scales (Figures 2c and 5). Diopside-rich layers are made of antigorite, two generations of diopside (Di1 and Di2), magnetite, chlorite, calcite and pentlandite ± ilmenite, hydroandradite, tremolite and talc. It must be noted that olivine is usually absent in diopside-rich layers (Figure 5a). The antigorites crystallized as lamellae of 50 to 200 µm in length oriented along rock foliation. They have Al_2O_3 contents ranging from 0.05 to 3.80 wt% and XMg values of 0.94-0.96 (Supplementary Table S1). Chlorite flakes can be observed in the centre of antigorite lamellae, sometimes completely replacing the latter (Figure 5c-d). These chlorite cores display Al_2O_3 contents ranging from 12.1 to 14.6 wt% and XMg values of 0.95, similar to those of antigorite. Rare and large diopside crystals (Di1) of up to 1 mm in length, often presenting kink band structures, are disseminated

334 within the antigorite matrix. They display mantle clinopyroxene like composition (e.g., Nozaka, 2010),
335 with Al_2O_3 contents of 1.7-6.7 wt%, Cr_2O_3 contents of 0.3-1.4 wt% and XMg values of 0.90-0.95. A
336 second generation of diopside (Di2) is either present as layers of about 300 µm in width orientated
337 along rock foliation (Figure 5a) or as small interstitial needles of 10-100 µm in length disseminated
338 within the antigorite matrix and orientated along rock foliation (Figure 5e-f). Di2 have lower Al_2O_3 (<
339 0.7 wt%) and Cr_2O_3 (<0.2 wt%) contents and higher XMg values (> 0.95) than those of Di1
340 (Supplementary Table S1). Di2 can be intimately associated with carbonates, most of the time calcite
341 but dolomite was also analysed in one sample (Figure 5b-d and Table 1). Carbonates is observed as
342 small indented veins crenulated along rock foliation (Figure 5b) and as porphyroclasts of hundreds of
343 micrometres (Figure 5d) to millimetre size (Figure 5c) embedded within rock foliation. The carbonates
344 are always overgrown by antigorite lamellae (Figure 5b, d). The calcite veins are associated with thin
345 coronas made of pentlandite, hydro-andradite, ilmenite and magnetite. The sheared tails of the
346 porphyroclasts are made of diopside (Di2), tremolite and talc (Figure 5c). At the contact with
347 porphyroclasts tails, the antigorite is partly to fully replaced by chlorite (Figure 5c-d). It is interesting
348 to note that both carbonate veins and porphyroclast rims are associated with DCM. The associated
349 Raman spectrum is marked by two broad D and G bands at 1369 cm^{-1} and 1591 cm^{-1}, respectively,
350 identical to that observed in chloriteschists and meta-ophimagnesites (Figure 3).
351 Olivine-rich layers are made of granoblastic olivine (Ol2), magnetite, titanochondrodite (TiChn),
352 titanoclinohumite (TiCl), brucite, pentlandite and awaruite (Figure 5e-g). Granoblastic olivines
353 crystallized as grains of variable width ranging from 10 to 400 µm. They display low NiO content (below
354 detection limit up to 0.28 wt%) and XMg values (0.77 to 0.87, on average 0.82 in 15 analyses) relative
355 to mantle olivine (e.g., Nozaka, 2010). Brucite aggregates of up to 500 µm in width are observed within
356 olivine-rich layers in few samples (Table 1). Brucites have XMg values ranging from 0.92 to 0.94.
357 Olivines can be associated with large humite crystals of 300 µm in length (Figures 2c and 5e-f). Electron
358 microprobe analyses show that these crystals are highly heterogeneous, having compositions
359 spreading between titanochondrodite and titanoclinohumite endmembers. This agrees with previous

studies that have shown that both humite varieties can be associated at micrometric scales in HP-serpentinites (e.g., López Sánchez-Vizcaíno et al., 2005). Titanochondrodites have TiO_2 contents ranging from 6.18 to 7.80 wt% and XMg^{TiChn} values from 0.85 to 0.86 ($XMg^{TiChn/TiCl}$=Mg/(Mg+Fe+Mn+Ni)). Titanoclinohumites have TiO_2 contents ranging from 4.32 to 7.01 wt% and XMg^{TiCl} values from 0.85 to 0.90. Titanochondrodites and titanoclinohumites are chlorine and fluorine-free (Supplementary Table S1). Olivines are also intimately associated with small interstitial magnetite crystals and large automorphic pentlandite (about 50µm in width) and/or awaruite (50-100 µm in width; Figure 5g).

5.4 Lower Shear Zone serpentinites

LSZ-serpentinites were sampled in the southern part of the Monviso massif in the Lower Shear Zone separating metabasites and basal serpentinites. These rocks are composed of an alternance of antigorite-rich and olivine-rich layers (Figure 6a) forming sigmoidal plans, contributing to a S-C fabric at the sample and thin section scales (Figure 2e, see Schwartz et al., 2013 for more details). The antigorite-rich layers are made of orientated antigorite lamellae of 100 µm in length with Al_2O_3 contents ranging from 1.5 to 1.9 wt% and XMg values of 0.96 (Supplementary Table S1). The olivine-rich layers are made of olivine (Ol2), magnetite, brucite, titanoclinohumite, pentlandite and awaruite. Olivines crystallized as grains of variable width, from 20 µm to 400 µm. They have similar XMg values of 0.84 – 0.88 and low NiO contents (<0.12 wt%) (Figure 6a). Brucite is observed as patches composed of lamellae of about 200 µm in length and surrounded by small grains of Ol2 of about 20 µm in width. Brucites have high XMg values ranging from 0.94 to 0.97. They are closely associated with magnetite grains of about 400 µm in width. Titanoclinohumite crystallized as small grains of about 50 µm disseminated within olivine-rich layers. They have TiO_2 contents of ~6.2 wt%, XMg^{TiCl} values of ~0.90, and are fluorine and chlorine-free (Supplementary Table S1). Awaruite crystals of 50 µm in width and pentlandite grains of 100 µm are observed surrounding magnetite (Figure 6b). Some massive serpentinite blocks have preserved early oceanic-like textures such as mesh and bastite textures replacing mantle olivine and pyroxenes, respectively (Supplementary Figure S1). These textures are

crosscut by chrysotile veins. Mantle olivines in LSZ-serpentinites have higher NiO contents compared to Ol2, ranging from 0.31 to 0.46 wt%. They have a XMg value of 0.89.

Meta-ophidolomites were sampled in both the USZ and the LSZ, near the Rifugio Quintino Sella. They consist of an alternance of dolomite-rich and diopside-rich layers interbedded by antigorite. Antigorite lamellae of about 100 µm in length display Al_2O_3 contents ranging from 1.4 to 2.2 wt% and XMg values of 0.94 (Supplementary Table S1). The dolomite-rich layers are made of dolomite crystals of up to 1 cm in width surrounded by metamorphic coronas made of diopside (Di2) or calcite and magnetite. It must be noted that Gilio et al. (2020) also reported the existence of meta-ophimagnesites within the LSZ; those were not studied here.

5.5 Basal serpentinites

Basal serpentinites were sampled in the northern part of the Monviso massif near Villanova and the Rifugio Barbara Lowrie. These rocks are made of an alternance of antigorite- and olivine-rich layers (Figure 2d). They are composed of antigorite, metamorphic olivines, magnetite, brucite, chlorite, heazlewoodite and rare diopside (Di1 and Di2) (Figure 7). In antigorite-rich layers, antigorites crystallize as lamellae of 100 µm in length orientated along rock foliation. Their Al_2O_3 contents range from 1.2 to 2.1 wt% and their XMg values from 0.96 to 0.98 (Supplementary Table S1). Antigorites are intimately associated with thinly crystalized (<10 µm width) olivine and micrometric grains of magnetite (Figure 7a-b), giving a dusty aspect in thin sections (Figure 7a). Dusty olivines display NiO contents ranging from 0.03 to 0.22 wt% and XMg values ranging from 0.90 to 0.94. Chlorites, which have XMg values of 0.95, crystallized as orientated lamellae of 200 µm in length displaying a strong zoning, with a brown core and a dark blue rim. Brown chlorites are also observed in the centre of antigorite lamellae (Figure 7b). Rare brucites crystallize as small flakes of 100 µm in length aggregated within patches (Figure 7b). They display XMg values of about 0.97. The contact between brucites and antigorites is always underlined by dusty olivine/magnetite assemblages (Figure 7b). Rare diopsides are also observed either as (i) isolated crystals of about 400 µm in width (Di1), deformed along the foliation and sometimes presenting kink band structures or (ii) large crystals of 200 µm in width with a brown colour

and numerous inclusions of magnetite (Di2). Di2 are Al_2O_3 and Cr_2O_3 free (< 0.1 wt%) and have XMg values of about 0.97-0.98. Olivine-rich layers are mainly made of euhedral olivine crystals (Ol2) of about hundreds of micrometres in width containing numerous fluid, andradite and antigorite inclusions (Figures 7c). Euhedral olivines display low NiO contents (0.02-0.14 wt%) and high XMg values (0.96-0.97) compared to dusty olivines (Figure 7a). Large magnetite and heazlewoodite crystals of 50 µm in width are also observed associated with euhedral olivines (Figure 7d).

6. Temperature and redox record along the massif

6.1 Homogeneous temperature record

The Monviso meta-ophiolite has long been considered as a fossilized serpentinite subduction channel, resulting in the formation of tectonic melanges (Blake et al., 1995; Guillot et al., 2004; Schwartz et al., 2001). However, more recent studies have revised this model suggesting that it consists of two main coherent tectonometamorphic subunits, namely the Upper and Lower Tectonic Units (Figure 1), detached at different depths during subduction and later juxtaposed during exhumation along the subduction interface (Angiboust et al., 2012). The existence of two coherent tectonic subunits is notably supported by a good homogeneity of metamorphic peak temperatures recorded within each subunit (Angiboust et al., 2012; Gilio et al., 2020; Locatelli, Federico, et al., 2019; Locatelli, Verlaguet, et al., 2019). However, up to now, most of the metamorphic studies on the Monviso meta-ophiolite have investigated the southern part of the massif (e.g., Angiboust et al., 2012, 2014; Blake et al., 1995; Gilio et al., 2020; Groppo & Castelli, 2010; Guillot et al., 2004; Locatelli et al., 2018; Locatelli, Verlaguet, et al., 2019; Schwartz et al., 2001), while the northern part is the subject of only a few ones (Balestro et al., 2015, 2018). Although the continuation of tectonic structures from North to South remains unclear (Figure 1a), the temperatures obtained here on sedimentary organic matter by RSCM thermometry suggest a homogeneous temperature record for the metasedimentary rocks all along the massif with temperature estimates overlapping within an interval of 50°C (i.e., within the associated errors; Beyssac et al., 2002) from North to South (Figure 1).

The ultramafic rocks of the Lower Tectonic Unit are characterized by the occurrence of an antigorite-olivine ± brucite paragenesis from North to South (Figures 2, 5, 6 and 7). The granoblastic textures (Figures 6a, 7a-b), the presence of mineral inclusions, such as antigorite within olivine (Figure 7c), and the highly variable NiO contents and XMg values (Figure 8a) of olivines are coherent with a metamorphic origin, as already proposed by several studies on the southern part of the Monviso meta-ophiolite (Gilio et al., 2020; Schwartz et al., 2013). The preferential crystallization of olivine at the contact between brucite and antigorite (Figures 6a and 7b), as well as the rare occurrences of brucite in the studied samples (Table 1), suggest that metamorphic olivines formed after antigorite and brucite according to the following reaction in $MgO\text{-}SiO_2\text{-}H_2O$ systems (Evans, 2004; Schwartz et al., 2013):

(1) Brucite + Antigorite = Olivine + H_2O

$$Mg(OH)_2 + Mg_3Si_2O_5(OH)_4 = 2Mg_2SiO_4 + 3H_2O$$

In a system containing aluminium, brucite breakdown is also expected to stabilize chlorite, as supported by the observation of this mineral with antigorite and/or olivine in the studied samples (e.g., Figures 7b). Brucite breakdown was previously inferred to occur nearby 400°C at 2.0-2.5 GPa in $MgO\text{-}SiO_2\text{-}H_2O$ systems (Evans, 2004). However, new estimates in the $FeO\text{-}Al_2O_3\text{-}MgO\text{-}SiO_2\text{-}H_2O$ system extends the stability field of brucite up to 550°C (Kempf et al., 2020). In agreement with these previous studies, our P-T pseudosection calculations in the $CaO\text{-}FeO\text{-}MgO\text{-}SiO_2\text{-}H_2O$ system show that Eq. (1) can occur over a large range of temperatures in the Monviso meta-ophiolite, from 400 to 550°C at 2.3-2.7 GPa (Figure 9a and Supplementary Figure S2). These temperatures estimates are poorly sensitive to pressure and overlap with the metamorphic conditions recorded by carbonaceous matter in metasedimentary rocks (516-565°C; this study and Angiboust et al., 2012; Figure 1a) and calculated by thermodynamic modelling in metabasites (~550°C, 2.6–2.7 GPa; Angiboust et al., 2012). It must however be noted that olivine amounts are highly variable at either the sample (e.g., Figure 5), outcrop (Figure 2) or massif scale (Table 1), olivine being notably absent in diopside/tremolite-rich layers forming paleoseafloor serpentinites. Using thermodynamic calculations in the $CaO\text{-}FeO\text{-}MgO\text{-}SiO_2\text{-}H_2O$ system and compositional variations in bulk rock metaserpentinites, we identified two metamorphic

463 sequences during subduction. These are characterized by a climax paragenesis (520-570°C and 2.6-2.7
464 GPa) at either Olivine-Brucite-Antigorite (Figure 9a) or Diopside-Talc-Antigorite (Figure 9b). These
465 different metamorphic pathways can be attributed to variable amounts of brucite in metaserpentinites
466 during prograde metamorphism (Figure 9c). Brucite abundance in serpentinites is highly sensitive to
467 silica activity (Frost & Beard, 2007) and is therefore sensitive to SiO_2 abundance relative to MgO in bulk
468 rock and/or to the circulation of SiO_2-rich fluids in shear bands at HP. In agreement with previous
469 observations, Figure 9c shows that olivine appearance can be pushed up to 600-650°C (i.e., antigorite
470 breakdown) in SiO_2-rich systems, while it decreases to 480-490°C in MgO-rich systems. However, in
471 these models, the diopside modal amount is controlled by CaO concentrations in metaserpentinites,
472 which are poorly variable in mantle peridotite (0-4 wt%; (Bodinier & Godard, 2013). Hence, such
473 models cannot account for large variations of diopside modal amount and CaO variations (from 0.1 to
474 9 wt%) observed in bulk rock (Supplementary Table S2) at the massif scale, calling for other sources of
475 CaO and reactional pathways. In fact, a variation of carbon dioxide activity ($a CO_2$) also favours the
476 formation of diopside and talc at the expense of carbonates and antigorite in ultramafic systems
477 (Figure 9d). It is therefore plausible that the high amount of metamorphic diopside (Di2) found in
478 metaserpentinites reflects carbonated paleo-horizons (i.e., meta-ophicalcites) in the massif
479 subsequently devolatilize during subduction (see section 6.3 for more details about carbonate role
480 during brucite breakdown). Such an observation is coherent with Balestro et al. (2018) that argued for
481 the preservation of ODF paleo-structures in the northern part of the massif.
482 Few robust thermodynamic constrains on pressure exist within ultramafic rocks. However, the
483 observation of both titanoclinohumite and titanochondrodite (this study, e.g., Figures 2c and 5e-f, as
484 well as Gilio et al., 2020) is coherent with a HP equilibration above 2 GPa (Shen et al., 2014). For Gilio
485 et al. (2020), the absence of titanoclinohumite in LSZ-serpentinites suggests that these rocks
486 equilibrated below Eq. (1) curve (T < 500°C; Figure 9c) during the Monviso retrograde path. However,
487 the stability of titanoclinohumite phases are also controlled by TiO_2 concentrations in the protolith,
488 TiO_2 mobility in fluids, carbonate activity and F concentrations (Evans & Trommsdorff, 1983; Savko &

489 Skryabin, 1999). All of these parameters being unknown and likely variable at the massif scale, the
490 variable occurrence of humite phases is more likely to reflect chemical heterogeneities than a
491 variability of pressure recorded in the metaserpentinites.
492 Overall, from North to South, temperature estimates based either on metasedimentary rocks,
493 metabasites and metaserpentinites overlap within a range of 50°C suggesting that the different
494 lithologies composing the Lower Tectonic Unit recorded homogeneous P-T conditions, with a
495 metamorphic climax nearby 520-570°C and 2.6-2.7 GPa. Our observations further support previous
496 studies (Angiboust et al., 2012, 2014; Gilio et al., 2020; Locatelli et al., 2018; Locatelli, Verlaguet, et al.,
497 2019) showing that the Monviso constitutes a large oceanic lithosphere section eclogitized during
498 subduction and partly dismembered during Alpine orogeny. The Monviso lithostratigraphic sequence
499 includes, from East to West, a succession of deep-seated lithologies, including gabbroic intrusions into
500 an extended section of serpentinized lithospheric mantle (i.e., basal serpentinites), to paleoseafloor
501 lithologies, including metasediments sitting on serpentinites in the North or metabasalts sitting on
502 metagabbros in the South. This sequence is coherent with the preservation of a heterogeneous crustal
503 section such as the ones observed at slow-spreading ridges (Cannat, 1995) or in other Western Alps
504 (meta-)ophiolites (Lagabrielle & Cannat, 1990).

505 ## 6.2 A contrasted redox record in metaserpentinites

506 Although they result from the same metamorphic reaction (Eq. 1), metamorphic olivines display highly
507 variable NiO contents (below detection limit up to 0.28) and XMg values (0.77-0.97) along the massif
508 (Figure 8a and Supplementary Table S1). The low NiO contents in Monviso olivines relative to mantle
509 olivine are typical of metamorphic processes (Nozaka, 2010). Also relative to mantle olivines, olivines
510 from basal serpentinites have higher XMg values, up to 0.97, while olivines from paleoseafloor and
511 LSZ-serpentinites have lower and extremely variable XMg values, down to 0.77. Kempf et al. (2020)
512 ascribe XMg value variations in metamorphic olivine to variable temperatures of crystallization during
513 brucite breakdown, where Fe-rich olivine becomes progressively more Mg-rich with increasing
514 temperature. These authors report XMg value variations between 0.93 and 0.97 in the Zermatt-Saas

515 eclogitic meta-ophiolite (Swiss Alps). The highest XMg values (nearby 0.97) are ascribed to
516 metamorphic vein crystallization equilibrated with metamorphic fluids, while XMg value variations in
517 host rock olivines (in the range 0.93 to 0.96) are ascribed to a narrow temperature range, between 10
518 to 20°C. Similar XMg value variations between metamorphic veins and host rock olivines are observed
519 in the Monviso basal serpentinites (Figure 7a). However, according to Kempf et al. (2020)
520 thermometer, a jump in temperature of about 75°C and up to 150°C is required to account for XMg
521 value variations from 0.77 to 0.94 at 2.6 GPa in the whole massif (Figure 9a). This is not consistent with
522 the apparent homogeneous P-T recorded by associated metasedimentary rocks and metabasites
523 (Figure 1). Similarly, such XMg dependency on temperature suggests that only the first stages of brucite
524 breakdown may produce XMg values lower than 0.85 (Kempf et al., 2020), while in the Monviso meta-
525 ophiolite, olivine with low XMg values were analysed in several samples presenting high modal amount
526 of metamorphic olivines (Figure 8a-b), calling for other processes. Interestingly, the accessory phases
527 associated with metamorphic olivines composing paleoseafloor and LSZ- serpentinites are made of
528 pentlandite and awaruite (Figures 5g and 6b), while heazlewoodite and magnetite are present in basal
529 serpentinites (Figure 7d). Pentlandite, awaruite, heazlewoodite and magnetite appearance are
530 primarily controlled by fO_2 and/or fS_2 variations and Fe partitioning between metamorphic phases
531 rather than variations in P or T (Evans et al., 2017). In order to better characterized Fe exchanges
532 between silicates, Fe-oxides, Ni/Fe-alloys and sulfides, we attempted to model brucite breakdown in
533 the S-NiO-CaO-FeO-MgO-SiO_2-H_2O system (Figure 10). In these models, pentlandite and awaruite can
534 only be equilibrated at low oxygen fugacity (<-27 log(fO_2); ~ FMQ -4; Figure 10), which agrees with
535 previous thermodynamic studies (Evans et al., 2017). At such conditions, the presence of awaruite and
536 pentlandite during brucite breakdown leads to low-Ni olivine, as shown by NiO content in olivine
537 isopleths (Figure 10) and in accordance with the low NiO contents of metamorphic olivines composing
538 the paleoseafloor and LSZ- serpentinites, overall suggesting that these phases crystallized at
539 equilibrium. In contrast, basal serpentinites forming olivines display relatively high NiO contents and
540 are associated with magnetite and heazlewoodite. These rocks are also characterized by the absence

of awaruite, which, according to thermodynamic calculations, requires lower fO_2 conditions, i.e., log(fO_2) around -24 (~ FMQ; Figure 10). Pseudosections show that the disappearance of awaruite leads to an increase of NiO contents in olivines, explaining the high NiO concentrations in olivine formed in basal serpentinites relative to paleoseafloor and LSZ- serpentinites (Figure 8a). This therefore suggests that paleoseafloor, LSZ- and basal serpentinites have recorded a strong redox gradient, varying from around -27 to-22 log(fO_2). These redox variations also influence the fate of magnetite during brucite breakdown and therefore the XMg value variations of metamorphic olivines (XMg values isopleths in Figure 10). Paleoseafloor and LSZ- serpentinites preserved interstitial magnetite and automorphic awaruite and pentlandite (e.g., Figure 5g). This textural relationship suggests that olivine, awaruite and pentlandite are concomitantly formed during brucite breakdown, while the interstitial magnetite could represent the last steps of brucite breakdown, associated with a decrease of rock porosity and the precipitation of the less fluid mobile elements such as Fe. Similarly, the observation of both awaruite and pentlandite surrounding large magnetite crystals (Figure 6b) also suggests that magnetite is poorly stable during brucite breakdown in these lithologies and at low fO_2 conditions, as predicted by thermodynamic calculations (Figure 10). At the opposite, in basal serpentinites, magnetite is abundant (Figure 7) and olivine displays relatively high XMg values and NiO contents (Figure 8a-b) coherent with high fO_2 conditions (Figure 10). Hence, as shown by thermodynamic models, XMg isopleths are controlled by fO_2 conditions, with Olivine-Antigorite-Heazlewoodite-Magnetite assemblages being equilibrated with XMg values of 0.89-0.93, while Olivine-Antigorite-Pentlandite-Awaruite assemblages are equilibrated over a large range of lower XMg values, from 0.77 to 0.85 (Figures 10).

6.3 Role of carbon during redox variations accompanying serpentinite dehydration at high pressure

The Monviso ultramafic rocks are associated with different types of carbonates, namely calcite, magnesite and dolomite (e.g., Figure 2b, 4b, d, 5b, c and Table 1), reflecting different stages of carbon mobilisation along the massif history (e.g., Gilio et al., 2020). Here we discuss carbonate origin and metamorphic reactions leading to carbonate destabilization during either subduction- (prograde)

and/or exhumation- (retrograde) related metamorphism. We also link the different stages of carbonate devolatilization to the precipitation of DCM during the evolution in pressure and temperature of the massif.

6.3.1 Abyssal calcite destabilization during prograde metamorphism

As shown by thermodynamic modelling (Figure 9d), the presence of carbonate in paleoseafloor serpentinites is likely to influence the metamorphic reaction pathways during subduction. In the Monviso meta-ophiolite, rare calcite relicts are observed as crenulated veins (Figure 5a-b), porphyroclasts embedded in rock foliation (Figure 5c-d) or in the centre of diopside-rich layers (Figure 4b) in both paleoseafloor serpentinites and chloriteschists. These textural relationships show that the formation of calcite occurred prior to Alpine-related deformation and metamorphism. Indeed, calcites are commonly observed close to the seafloor in abyssal settings and are interpreted as paleoseafloor related in ophiolites (Lafay et al., 2017) when they are associated with sediments and serpentinites (referred as the "Steinman trinity" in Alpine meta-ophiolites, see Bernoulli et al., 2003 for a review). During subduction, calcite is unlikely to form in ultramafic systems as the precipitation of metamorphic Ca-bearing silicates (e.g., diopside or tremolite) controls the chemical potential of Ca. This reduces the concentration of Ca in metamorphic fluids and therefore the stability and the formation of HP-related meta-ophicalcites (Menzel et al., 2020). In agreement with thermodynamic modelling (Figure 9d), calcite porphyroclasts are surrounded by complex reaction rims made of diopside (and/or tremolite), talc, magnetite and chlorite (Figures 4b, 5c-d). The diopside (Di2) observed either in paleoseafloor serpentinites or chloriteschists display low Al_2O_3 and Cr_2O_3 contents and high XMg values relative to large kink band diopside crystals (Di1; Figure 8b), coherent with a metamorphic origin. The formation of chloriteschists and diopside-rich layers in paleoseafloor serpentinites can therefore be explained by a progressive decrease in aCO_2 favouring the formation of diopside-magnetite-chlorite at the expense of carbonate and antigorite (Debret et al., 2018). Indeed, the large amount of fluids released during brucite breakdown at HP can induce such a decrease in aCO_2 in fluids and therefore enhance calcite

592 dissolution (Kelemen & Manning, 2015). This can be expressed in the Monviso meta-ophiolite
593 according to the simplified reaction:

594 (2) Brc + Atg + Cal = Mt + Di + $3H_2O_{(aq)}$ + $CO_{X(aq)}$

595 $(Mg,Fe)(OH)_2 + (Mg,Fe)_3Si_2O_5(OH)_4 + CaCO_3 = Fe_3O_4 + CaMgSi_2O_6 + 3H_2O_{(aq)} + CO_{X(aq)}$

596 Additional Al_2O_3 component that can be present in antigorite will allow chlorite formation as shown
597 by the occurrence of flakes made of chlorite at the contact of diopside-rich layers (Figures 4a-b and
598 5ad). Brucite breakdown in carbonate-rich lithologies is therefore expected to stabilize a chlorite-
599 diopside/tremolite-magnetite paragenesis at HP.
600 Considering the reasoning above, the chloriteschists made of an alternance of diopside- and chlorite-
601 rich layers preserving level of calcite in their centre (Figure 4a-b) can be interpreted as former seafloor-
602 related ophicarbonate horizons formed at the contact between metasedimentary rocks and
603 serpentinites (Figure 1) and partly to fully devolatilized at HP during brucite breakdown. This is in good
604 agreement with recent observations in the Queyras meta-ophiolites where diopside-rich serpentinites
605 are also interpreted as meta-ophicarbonates (Debret et al., 2018). In Eq. (2), the exact form of carbon
606 in fluids is highly speculative as this is intimately related to fO_2 conditions at HP, with reduced
607 conditions possibly favouring the abiotic formation of organic compounds (e.g., hydrocarbons
608 including methane or organic acids such as formate, $HCOO^-$) at the expense of carbonates (Sverjensky
609 et al., 2014; Vitale Brovarone et al., 2017).
610 The formation of organic compounds during decarbonation reactions is consistent with the redox
611 record of carbonate free paleoseafloor serpentinites found at the contact with meta-ophicalcites and
612 chloriteschists (Figure 10). It is indeed interesting to note that diopside and chlorite in carbonated
613 paleoseafloor serpentinites and chloriteschists are intimately associated with DCM (Figure 4c),
614 characterized in Raman spectroscopy by a broad D band with relatively high intensity compared to the
615 associated G band (Figure 3). Given the close spatial association of DCM with this paragenesis, it seems
616 reasonable to propose that DCM results from abyssal calcite devolatilization at HP-HT during
617 subduction. The thermal maturation of organic matter during subduction is usually yet misleadingly

simplified to kerogen (i.e., insoluble macromolecular organic matter of biological origin dispersed in sedimentary rocks) graphitization upon burial through thermal cracking (allowing C-C bond breaking), as described by Beyssac et al. (2002) for metasedimentary rocks. This is typically associated with the progressive structural evolution of poorly-ordered C-, O-, H-bearing kerogens starting at low temperatures, until the formation of pure C-bearing and well-ordered graphite at 600-700°C (Vandenbroucke & Largeau, 2007). However, the observed DCM preserved here a large amount of structural disorder (Figure 3) which is not compatible with a biological origin and a kerogen like evolution during subduction, therefore calling for new reaction pathways and revisited stability considerations when serpentinite-hosted organic matter is considered. Indeed, recent natural observations have shown that abiotic organic compounds with pure aliphatic structure, i.e., opposed to aromatic graphite-like structure, can be stable and formed at HP-HT in subduction settings (Debret et al., 2022). This suggest that a large diversity of organic compounds of not only biological origin but also formed through HP-HT abiotic processes might exist in subduction zones. However, the mechanisms and diversity of these abiotic solid organic compounds remain at that time poorly investigated. Toffolo et al. (2023) show that the solubility of carbonaceous matter at HP-HT is related to its structure and properties (e.g., oxygen heteroatoms, presence of oxygenated functional groups), with oxidizing conditions and high fluid/rock ratio favouring the dissolution of DCM in fluids. In agreement with this, the experiments of Szlachta et al. (2022) show that acetate, which is thermodynamically predicted at HP-HT under reduced conditions (e.g., Sverjensky et al., 2014), is unlikely to be stable in fluids but rather decomposes to a disordered graphite-like material, with a Raman spectral signature similar to that observed for DCM at the Monviso meta-ophiolite. Similarly, Tao et al. (2018) report the formation of abiotic hydrocarbons and graphite through the reduction of siderite under low fO_2 conditions at 1-6 GPa and 600-1200°C. It is important to note that the graphite-associated Raman spectra reported in Tao et al. (2018) display an important structural disorder which might correspond to DCM or graphitic carbon rather than pure graphite. These results show that solid organic carbon phases could be formed through various processes (i.e., fluid saturation and

644 dissociation of organic compounds or redox processes) along prograde metamorphic pathway in
645 subduction zones. The low fO_2 recorded by paleoseafloor serpentinites and associated chloriteschists
646 could therefore have favoured the preservation and/or the formation of DCM during subduction.

647 ### 6.3.2 Meta-ophimagnesites and meta-ophidolomites

648 Meta-ophimagnesites and meta-ophidolomites form large boudins embedded within the foliation of
649 chloriteschists and LSZ-serpentinites in the northern and southern part of the massif, respectively (e.g.,
650 Figure 2b). Relative to calcite, both magnesites and dolomites are abundant at the massif scale.
651 According to Gilio et al. (2020), the formation of magnesite in the Monviso meta-ophiolite is attributed
652 to subduction-related processes occurring close to metamorphic climax. The same authors report
653 magnesite overprint by dolomite suggesting that dolomite crystallized during massif exhumation. They
654 also report in these rocks the occurrence of minor calcite veins crosscutting rock foliation and attesting
655 for the existence of a second generation of calcite crystallizing during the late stages of massif
656 exhumation.

657 It is interesting to note that magnesite crystals display complex metamorphic rims made of dolomite,
658 magnetite, chlorite, talc, tremolite or diopside (Figure 4d). The stabilization of talc, tremolite or
659 diopside within these metamorphic rims is mainly controlled by aCO_2 rather than P-T conditions (Figure
660 9d), with decreasing aCO_2 leading to the successive formation from talc + carbonate, to tremolite +
661 carbonate, diopside + carbonate until diopside alone (Debret et al., 2018). This suggests successive
662 carbonate leaching and re-precipitation episodes along the massif metamorphic history. These are
663 probably controlled by external fluid circulation along rheological interfaces between different
664 lithologies (e.g., LSZ and/or ODF; Figure 1). Moreover, diopside and chlorite in magnesite metamorphic
665 rims are associated with DCM (Figure 4c) showing that the successive episodes of carbonate leaching,
666 releasing CO_2 in metamorphic fluids, participate to a progressive decrease of both aCO_2 and fO_2 within
667 meta-ophimagnesites, allowing during the last stages (i.e., diopside precipitation) the reduction of
668 carbonate into DCM.

6.4 Origin of slab redox gradient

Sulfide and Ni-Fe alloys assemblages are key indicators of fO_2 conditions (Evans et al., 2017). In the Monviso serpentinites, they shift from magnetite-pentlandite-awaruite assemblages (indicative of low fO_2) in paleoseafloor lithologies to magnetite-heazlewoodite assemblages (indicative of high fO_2) in the deep-seated lithologies. Both assemblages coexist with metamorphic olivines and are likely equilibrated nearby massif climax at 520-570°C and 2.6-2.7 GPa (Figure 10). This shows the existence of a redox gradient affecting the Monviso oceanic lithosphere at HP-HT during subduction. It has been suggested that pre-subduction composition of serpentinites have major implications on the fO_2 evolution during subduction, notably that sulfur- and nickel-bearing phases exercise a major control of fO_2 variations (Debret & Sverjensky, 2017; Evans et al., 2017; Evans & Frost, 2021; Evans & Powell, 2015; Iacovino et al., 2020; Lazar, 2020; Maurice et al., 2020; Vieira Duarte et al., 2021). In abyssal settings, deep-seated serpentinites generally display high sulfur and sulfide (mainly as pentlandite, pyrrhotite and pyrite) contents (Alt et al., 2013) due to interactions between metagabbros/serpentinites and fluids. In contrast, serpentinites formed near the seafloor (or nearby ODF) are expected to be equilibrated at higher fO_2 conditions and tend to display low amount of sulfur, mostly in the form of sulfates (Alt et al., 2013; Delacour et al., 2008). Similarly, partially serpentinized peridotites composing the deep part of the oceanic lithosphere are likely to form abundant brucite and serpentine associated with pentlandite, magnetite and awaruite (Schwarzenbach et al., 2016), while both brucite and awaruite disappear near the seafloor under oxidizing conditions associated with the abundant percolation of seawater, which is furthermore undersaturated with respect to brucite (Frost & Beard, 2007; Klein et al., 2020). Overall, this suggests the formation of assemblages equilibrated at relatively low fO_2 at depth and assemblages equilibrated at higher fO_2 toward the seafloor. These observations are opposite to what is observed in the Monviso meta-ophiolite suggesting that the observed redox gradient cannot be inherited from an abyssal stage at mid-ocean ridges and must have been settled during Alpine subduction.

694 The dehydration of serpentinites has the potential to lead to a significant increase of fO_2 conditions up
695 to the total dissolution of sulfides in the presence of metamorphic fluids (e.g., Debret & Sverjensky,
696 2017; Maurice et al., 2020; Evans & Frost, 2021). Although sulfides are still preserved in Monviso
697 metaserpentinites, the co-existence of magnetite and heazlewoodite within basal serpentinite
698 dehydration products agrees with an increase of fO_2 during subduction. Similarly, the presence of
699 heazlewoodite in metamorphic veins also suggests that sulfur is mobilized in fluids equilibrated at high
700 fO_2 during subduction. In contrast, the presence of carbonate in paleoseafloor serpentinites
701 harbouring pentlandite and awaruite tends to buffer the fO_2 at lower level during brucite breakdown.
702 The role of carbonate can be illustrated through the decarbonation reactions Eq. (2) in lithologies
703 composing the metasomatic contact between metaserpentinites and metasedimentary rocks in the
704 Monviso meta-ophiolite. In these carbonated interfaces, the progressive leaching of carbonate in
705 serpentinite derived fluids decreases meta-ophicarbonate redox budget, ultimately leading to a
706 decrease of both aCO_2 and fO_2 nearby seafloor lithologies. It therefore suggests that carbon plays a
707 major role on fO_2 conditions in subducting slab, notably contributing to the emplacement of an inverse
708 redox gradient in the Monviso meta-ophiolite. Interestingly, the observation of solid organic
709 compounds' horizons forming from carbonate under reduced conditions at the contact between
710 serpentinites and metasedimentary rocks (this study and also Galvez et al., 2013; Vitale-Brovarone et
711 al., 2017) shows that these reactions can promote organic carbon formation. These transformations
712 have therefore the potential to affect long term carbon recycling, favouring the transfer of organic
713 carbon to the deep mantle in the form of DCM.
714 Redox variations during serpentinite dehydration were also described in other eclogitic meta-
715 ophiolites, sometimes leading to apparently contrasted conclusions (e.g., Debret & Sverjensky, 2017;
716 Piccoli et al., 2019). As an illustration, in the Lanzo massif (Western Alps), Debret et al. (2016) show
717 that the dehydration of serpentinites can be accompanied by hematite formation suggesting fO_2
718 conditions close to FMQ +3 to +4. In the same meta-ophiolite, Vitale-Brovarone et al. (2017) highlight
719 the formation of graphite and methane rich fluid inclusions in paleoseafloor lithologies (i.e., meta-

ophicarbonates), compatible with highly reducing conditions, close to FMQ -4. These apparently contrasted observations can be reconciled by the existence of a redox gradient affecting the lithosphere at HP, such as the one observed here in the Monviso meta-ophiolite. Indeed, the metamorphic olivine of the Lanzo massif also display large XMg variations (from 0.79 to 0.90; Debret et al., 2013; Figure 11), compatible with heterogenous redox conditions at HP-HT during serpentinite dehydration. It must be noted that such variability in metamorphic olivine composition is not observed for all Alpine meta-ophiolites. For example, metamorphic olivines from Zermatt, Cerro del Almirez and Erro Tobbio massifs show relatively homogeneous composition (Figure 11). However, large variations of XMg values in metamorphic olivines are observed at the scale of the Alps, passing from one meta-ophiolite setting to another. Given that these massifs have recorded similar temperature conditions (Agard, 2021), such variations might support heterogeneous redox record, therefore calling for further investigations.

7. Conclusion

We show that the different lithologies (i.e., metasedimentary rocks, metabasites and metaserpentinites) composing the Lower Tectonic Unit of the Monviso meta-ophiolite recorded homogeneous P-T conditions (nearby 520-570°C and 2.6-2.7 GPa) from South to North confirming that the massif constitutes a coherent tectonic unit subducted to eclogite facies P-T conditions during Alpine subduction. Despite a homogeneous P-T record, serpentinites display variable metamorphic assemblages reflecting a redox gradient affecting the massif from East to West. This gradient is probably set up during serpentinite dehydration near metamorphic climax, with basal serpentinites composing the eastern part of the massif recording higher fO_2 conditions relative to paleoseafloor serpentinites associated with meta-ophicarbonates and chloriteschists. This redox gradient is linked to the presence of carbon-bearing phases near the paleoseafloor that buffer down the fO_2 through decarbonation redox reactions, thus confirming that the presence of redox sensitive elements in the initial lithology of the oceanic lithosphere has major implications on the evolution of fO_2 during

subduction. A decoupling of carbon behaviour is possible (e.g., Bouilhol et al., 2022), as (i) oxidized carbon-bearing fluids are likely to be leached toward to the mantle wedge after serpentinite dehydration and (ii) the progressive decrease in fO_2 expected through decarbonation redox reactions can potentially form and/or stabilize inherited endogenous carbonaceous compounds atHP and their preferential recycling to the deep mantle.

Acknowledgements

The authors thank H. Beunon and N. Mattielli for their assistance during the 2018 field campaign, N. Rividi and M. Fialin for their assistance during electron microprobe analyses, as well as S. Borensztajn for SEM imaging. This study was supported by a CNRS grant from the Institut National des Sciences de l'Univers (INSU), by the LabEx UnivEarthS (ANR-10-LABX-0023 and ANR-18-IDEX-0001) and by the Agence Nationale de la Recherche (ANR) CARBioNic "ANR-22-CE49-0001-01". Part of this work was also supported by IPGP multidisciplinary program PARI, and by Region Ile-de-France SESAME grants no. 12015908 and EX047016.

References

Agard, P. (2021). Subduction of oceanic lithosphere in the Alps: Selective and archetypal from (slow-spreading) oceans. *Earth-Science Reviews*, *214*, 103517. https://doi.org/10.1016/j.earscirev.2021.103517

Alt, J. C., Schwarzenbach, E. M., Früh-Green, G. L., Shanks, W. C., Bernasconi, S. M., Garrido, C. J., et al. (2013). The role of serpentinites in cycling of carbon and sulfur : Seafloor serpentinization and subduction metamorphism. *Lithos*, *178*, 40–54. https://doi.org/10.1016/j.lithos.2012.12.006

Angiboust, S., Langdon, R., Agard, P., Waters, D., & Chopin, C. (2012). Eclogitization of the Monviso ophiolite (W. Alps) and implications on subduction dynamics. *Journal of Metamorphic Geology*, *30*(1), 37–61. https://doi.org/10.1111/j.1525-1314.2011.00951.x

Angiboust, S., Pettke, T., De Hoog, J. C. M., Caron, B., & Oncken, O. (2014). Channelized fluid flow and eclogite-facies metasomatism along the subduction shear zone. *Journal of Petrology*, *55*(5), 883–916. https://doi.org/10.1093/petrology/egu010

Balestro, G., Fioraso, G., & Lombardo, B. (2011). Geological map of the upper Pellice Valley (Italian Western Alps). *Journal of Maps*, *7*(1), 634–654. https://doi.org/10.4113/jom.2011.1213

Balestro, G., Fioraso, G., & Lombardo, B. (2013). Geological map of the Monviso massif (Western Alps). *Journal of Maps*, *9*(4), 623–634. https://doi.org/10.1080/17445647.2013.842507

Balestro, G., Festa, A., Dilek, Y., & Tartarotti, P. (2015). Pre-alpine extensional tectonics of a peridotite-

776 localized oceanic core complex in the late Jurassic, high-pressure Monviso ophiolite (Western
777 Alps). *Episodes*, *38*(4), 266–282. https://doi.org/10.18814/epiiugs/2015/v38i4/82421

778 Balestro, G., Festa, A., Borghi, A., Castelli, D., Gattiglio, M., & Tartarotti, P. (2018). Role of late jurassic
779 intra-oceanic structural inheritance in the alpine tectonic evolution of the Monviso meta-
780 ophiolite complex (Western Alps). *Geological Magazine*, *155*, 233–249.
781 https://doi.org/10.1017/S0016756817000553

782 Ballèvre, M., Lagabrielle, Y., & Merle, O. (1990). Tertiary ductile normal faulting as a consequence of
783 lithospheric stacking in the western Alps. *Mémoires de La Société Géologique de France*, *156*,
784 227–236.

785 Bernoulli, D, Manatschal, G., Desmurs, L., & Müntener, O. (2003). Where did Gustav Steinmann see
786 the trinity? Back to the roots of an Alpine ophiolite concept. In Y. Dilek & S. Newcomb (Eds.),
787 *Ophiolite concept and the evolution of geological thought* (Vol. 373, pp. 93–110). Boulder,
788 Colorado: Geological Society of America.

789 Beyssac, O., Goffé, B., Chopin, C., & Rouzaud, J. N. (2002). Raman spectra of carbonaceous material in
790 metasediments: A new geothermometer. *Journal of Metamorphic Geology*, *20*(9), 859–871.
791 https://doi.org/10.1046/j.1525-1314.2002.00408.x

792 Beyssac, O., Goffé, B., Petitet, J. P., Froigneux, E., Moreau, M., & Rouzaud, J. N. (2003). On the
793 characterization of disordered and heterogeneous carbonaceous materials by Raman
794 spectroscopy. *Spectrochimica Acta - Part A: Molecular and Biomolecular Spectroscopy*, *59*(10),
795 2267–2276. https://doi.org/10.1016/S1386-1425(03)00070-2

796 Blake, M. C., & Jayko, A. S. (1990). Uplift of very high pressure rocks in the western Alps : evidence for
797 structural attenuation along low-angle faults. *Mémoires de La Société Géologique de France*, *156*,
798 237–246.

799 Blake, M. C., Moore, D. E., & Jayko, A. S. (1995). The role of the serpentinite melange in the unroofing
800 of UHPM rocks: an example from western Alps of Italy. In R. G. Coleman & X. Wang (Eds.),
801 *Ultrahigh Pressure Metamorphism* (pp. 182–205). Cambridge, UK: Cambridge University Press.
802 https://doi.org/doi.org/10.1017/CBO9780511573088.007

803 Bodinier, J. L., & Godard, M. (2013). *Orogenic, Ophiolitic, and Abyssal Peridotites*. *Treatise on*
804 *Geochemistry: Second Edition* (3rd ed., Vol. 3). Elsevier Ltd. https://doi.org/10.1016/B978-0-08-
805 095975-7.00204-7

806 Bouilhol, P., Debret, B., Inglis, E., Burton, K. W., Warembourg, M., Grocolas, T., et al. (2022). Decoupling
807 of inorganic and organic carbon during slab mantle devolatilisation. *Nature Communications*, *13*,
808 308. https://doi.org/doi.org/10.1038/s41467-022-27970-0

809 Bretscher, A., Hermann, J., & Pettke, T. (2018). The influence of oceanic oxidation on serpentinite
810 dehydration during subduction. *Earth and Planetary Science Letters*, *499*, 173–184.
811 https://doi.org/10.1016/j.epsl.2018.07.017

812 Cannat, M. (1995). Thin crust, ultramafic exposures, and rugged faulting patterns at the Mid-Atlantic
813 Ridge (22°-24°N). *Geology*, *23*(1), 49–52. https://doi.org/10.1130/0091-
814 7613(1995)023<0049:TCUEAR>2.3.CO;2

815 Carignan, J., Hild, P., Mevelle, G., Morel, J., & Yeghicheyan, D. (2001). Routine analyses of trace
816 elements in geological samples using flow injection and low pressure on-line liquid
817 chromatography coupled to ICP-MS: A study of geochemical reference materials BR, DR-N, UB-N,
818 AN-G and GH. *Geostandards Newsletter*, *25*(2–3), 187–198. https://doi.org/10.1111/j.1751-
819 908x.2001.tb00595.x

Connolly, J. A. D. (2005). Computation of phase equilibria by linear programming: A tool for geodynamic modeling and its application to subduction zone decarbonation. *Earth and Planetary Science Letters*, *236*(1–2), 524–541. https://doi.org/10.1016/J.EPSL.2005.04.033

Connolly, J. A. D. (2009). The geodynamic equation of state: What and how. *Geochemistry, Geophysics, Geosystems*, *10*(10), 10014. https://doi.org/10.1029/2009GC002540

Connolly, J. A. D., & Cesare, B. (1993). C-O-H-S fluid composition and oxygen fugacity in graphitic metapelites. *Journal of Metamorphic Geology*, *11*(3), 379–388. https://doi.org/10.1111/J.1525-1314.1993.TB00155.X

Debret, B., & Sverjensky, D. A. (2017). Highly oxidising fluids generated during serpentinite breakdown in subduction zones. *Scientific Reports*, *7*, 10351. https://doi.org/10.1038/s41598-017-09626-y

Debret B., Nicollet C., Andreani M., Schwartz S. & Godard M. (2013). Three steps of serpentinization in an eclogitized oceanic serpentinization front (Western Alps). *Journal of Metamorphic Geology*, 31, 165-186.

Debret, B., Andreani, M., Muñoz, M., Bolfan-Casanova, N., Carlut, J., Nicollet, C., et al. (2014). Evolution of Fe redox state in serpentine during subduction. *Earth and Planetary Science Letters*, *400*, 206–218. https://doi.org/10.1016/j.epsl.2014.05.038

Debret, B., Bolfan-Casanova, N., Padrón-Navarta, J. A., Martin-Hernandez, F., Andreani, M., Garrido, C. J., et al. (2015). Redox state of iron during high-pressure serpentinite dehydration. *Contributions to Mineralogy and Petrology*, *169*(4), 36. https://doi.org/10.1007/s00410-015-1130-y

Debret, B., Bouilhol, P., Pons, M. L., & Williams, H. (2018). Carbonate transfer during the onset of slab devolatilization: new insights from Fe and Zn stable isotopes. *Journal of Petrology*, *59*(6), 1145–1166. https://doi.org/10.1093/petrology/egy057

Debret, B., Ménez, B., Walter, B., Bouquerel, H., Bouilhol, P., Mattielli, N., Pisapia, C., Rigaudier, T. & Williams, H. (2022). High-pressure synthesis and storage of solid organic compounds in active subduction zones. Science Advances 8, 37.

Delacour, A., Früh-Green, G. L., Bernasconi, S. M., & Kelley, D. S. (2008). Sulfur in peridotites and gabbros at Lost City (30°N, MAR): Implications for hydrothermal alteration and microbial activity during serpentinization. *Geochimica et Cosmochimica Acta*, *72*(20), 5090–5110. https://doi.org/10.1016/j.gca.2008.07.017

Ellis, D. J., & Green, D. H. (1979). An experimental study of the effect of Ca upon garnet-clinopyroxene Fe-Mg exchange equilibria. *Contributions to Mineralogy and Petrology*, *71*(1), 13–22. https://doi.org/10.1007/BF00371878

Evans, B. W. (2004). The serpentinite multisystem revisited: chrysotile is metastable. *International Geology Review*, *46*(6), 479–506. https://doi.org/10.2747/0020-6814.46.6.479

Evans, B. W., & Trommsdorff, V. (1983). Fluorine hydroxyl titanian clinohumite in Alpine recrystallized garnet peridotite: compositional controls and petrologic significance. *American Journal of Science*, *283A*, 355–369.

Evans, K. A., & Frost, B. R. (2021). Deserpentinization in subduction zones as a source of oxidation in arcs: A reality check. *Journal of Petrology*, *62*(3), egab016. https://doi.org/10.1093/petrology/egab016

Evans, K. A., & Powell, R. (2015). The effect of subduction on the sulphur, carbon and redox budget of lithospheric mantle. *Journal of Metamorphic Geology*, *33*(6), 649–670. https://doi.org/10.1111/jmg.12140

Evans, K. A., Reddy, S. M., Tomkins, A. G., Crossley, R. J., & Frost, B. R. (2017). Effects of geodynamic setting on the redox state of fluids released by subducted mantle lithosphere. *Lithos*, *278–281*, 26–42. https://doi.org/10.1016/j.lithos.2016.12.023

Festa, A., Balestro, G., Dilek, Y., & Tartarotti, P. (2015). A Jurassic oceanic core complex in the high-pressure Monviso ophiolite (western Alps, NW Italy). *Lithosphere*, *7*(6), 646–652. https://doi.org/10.1130/L458.1

Franzolin, E., Schmidt, M. W., & Poli, S. (2011). Ternary Ca-Fe-Mg carbonates: Subsolidus phase relations at 3.5 GPa and a thermodynamic solid solution model including order/disorder. *Contributions to Mineralogy and Petrology*, *161*(2), 213–227. https://doi.org/10.1007/s00410-010-0527-x

Frost, R. B., & Beard, J. S. (2007). On silica activity and serpentinization. *Journal of Petrology*, *48*(7), 1351–1368. https://doi.org/10.1093/petrology/egm021

Galvez, M. E., Beyssac, O., Martinez, I., Benzerara, K., Chaduteau, C., Malvoisin, B., & Malavieille, J. (2013). Graphite formation by carbonate reduction during subduction. *Nature Geoscience*, *6*, 473–477. https://doi.org/10.1038/ngeo1827

Gilio, M., Scambelluri, M., Agostini, S., Godard, M., Pettke, T., Agard, P., et al. (2020). Fingerprinting and relocating tectonic slices along the plate interface: Evidence from the Lago Superiore unit at Monviso (Western Alps). *Lithos*, *352–353*, 105308. https://doi.org/10.1016/j.lithos.2019.105308

Groppo, C., & Castelli, D. (2010). Prograde P-T evolution of a lawsonite eclogite from the Monviso meta-ophiolite (Western Alps): Dehydration and redox reactions during subduction of oceanic FeTi-oxide gabbro. *Journal of Petrology*, *51*(12), 2489–2514. https://doi.org/10.1093/petrology/egq065

Guillot, S., Schwartz, S., Hattori, K., Auzende, A., & Lardeaux, J. (2004). The Monviso ophiolitic massif (Western Alps), a section through a serpentinite subduction channel. *Journal of the Virtual Explorer*, *16*, 3. Retrieved from 10.3809/jvirtex.2004.00099

Holland, T. J. B., & Powell, R. (1998). An internally consistent thermodynamic data set for phases of petrological interest. *Journal of Metamorphic Geology*, *16*(3), 309–343. https://doi.org/10.1111/j.1525-1314.1998.00140.x

Holland, T. J. B., & Powell, R. (2003). Activity-compositions relations for phases in petrological calculations: An asymetric multicomponent formulation. *Contributions to Mineralogy and Petrology*, *145*(4), 492–501. https://doi.org/10.1007/S00410-003-0464-Z

Iacovino, K., Guild, M. R., & Till, C. B. (2020). Aqueous fluids are effective oxidizing agents of the mantle in subduction zones. *Contributions to Mineralogy and Petrology*, *175*(4), 36. https://doi.org/10.1007/s00410-020-1673-4

Kelemen, P. B., & Manning, C. E. (2015). Reevaluating carbon fluxes in subduction zones, what goes down, mostly comes up. *Proceedings of the National Academy of Sciences of the United States of America*, *112*(30), 3997–4006. https://doi.org/10.1073/pnas.1507889112

Kempf, E. D., Hermann, J., Reusser, E., Baumgartner, L. P., & Lanari, P. (2020). The role of the antigorite + brucite to olivine reaction in subducted serpentinites (Zermatt, Switzerland). *Swiss Journal of Geosciences*, *113*(1), 16. https://doi.org/10.1186/s00015-020-00368-0

Klein, F., & Bach, W. (2009). Fe-Ni-Co-O-S phase relations in peridotite-seawater interactions. *Journal of Petrology*, *50*(1), 37–59. https://doi.org/10.1093/petrology/egn071

Klein, F., Humphris, S.E. & Bach, W. (2020). Brucite formation and dissolution in oceanic serpentinite.

Geochemical Perspective Letters, 16, 1-5. doi: 10.7185/geochemlet.2035

Lafay, R., Baumgartner, L. P., Schwartz, S., Picazo, S., Montes Hernandez, G., & Vennemann, T. (2017). Petrologic and stable isotopic studies of a fossil hydrothermal system in ultramafic environment (Chenaillet ophicalcites, Western Alps, France): Processes of carbonate cementation. *Lithos*, *294–295*, 319–338. https://doi.org/10.1016/j.lithos.2017.10.006

Lagabrielle, Y., & Cannat, M. (1990). Alpine Jurassic ophiolites resemble the modern central Atlantic basement. *Geology*, *18*, 319–322. https://doi.org/10.1130/0091-7613(1990)018<0319:AJORTM>2.3.CO;2

Lazar, C. (2020). Using silica activity to model redox-dependent fluid compositions in serpentinites from 100 to 700 °C and from 1 to 20 kbar. *Journal of Petrology*, *61*(12), egaa101. https://doi.org/10.1093/petrology/egaa101

Locatelli, M., Verlaguet, A., Agard, P., Federico, L., & Angiboust, S. (2018). Intermediate-depth brecciation along the subduction plate interface (Monviso eclogite, W. Alps). *Lithos*, *320–321*, 378–402. https://doi.org/10.1016/j.lithos.2018.09.028

Locatelli, M., Verlaguet, A., Agard, P., Pettke, T., & Federico, L. (2019). Fluid pulses during stepwise brecciation at intermediate subduction depths (Monviso eclogites, W. Alps): First internally then externally sourced. *Geochemistry, Geophysics, Geosystems*, *20*(11), 5285–5318. https://doi.org/10.1029/2019GC008549

Locatelli, M., Federico, L., Agard, P., & Verlaguet, A. (2019). Geology of the southern Monviso metaophiolite complex (W-Alps, Italy). *Journal of Maps*, *15*(2), 283–297. https://doi.org/10.1080/17445647.2019.1592030

Lombardo, B., Nervo, R., Compagnoni, R., Messiga, B., Kienast, J., Mevel, C., et al. (1978). Osservazioni preliminari sulle ofioliti metamorfiche del Monviso (Alpi Occidentali). *Rendiconti Societa` Italiana Di Mineralogia e Petrologia*, *34*, 253–305.

López Sánchez-Vizcaíno, V., Trommsdorff, V., Gómez-Pugnaire, M. T., Garrido, C. J., Müntener, O., & Connolly, J. A. D. (2005). Petrology of titanian clinohumite and olivine at the high-pressure breakdown of antigorite serpentinite to chlorite harzburgite (Almirez Massif, S. Spain). *Contributions to Mineralogy and Petrology*, *149*(6), 627–646. https://doi.org/10.1007/s00410-005-0678-3

Maurice, J., Bolfan-Casanova, N., Demouchy, S., Chauvigne, P., Schiavi, F., & Debret, B. (2020). The intrinsic nature of antigorite breakdown at 3 GPa: Experimental constraints on redox conditions of serpentinite dehydration in subduction zones. *Contributions to Mineralogy and Petrology*, *175*(10), 94. https://doi.org/10.1007/s00410-020-01731-y

Menzel, M. D., Garrido, C. J., & Sánchez-Vizcaíno, V. L. (2020). Fluid-mediated carbon release from serpentinite-hosted carbonates during dehydration of antigorite-serpentinite in subduction zones. *Earth and Planetary Science Letters*, *531*, 115964. https://doi.org/https://doi.org/10.1016/j.epsl.2019.115964

Navrotsky, A., & Capobianco, C. (1987). Enthalpies of formation of dolomite and of magnesian calcites. *American Mineralogist*, *72*(7–8), 782–787.

Nozaka, T. (2010). A note on compositional variation of olivine and pyroxene in thermally metamorphosed ultramafic complexes from SW Japan. *OKAYAMA University Earth Science Report*, *17*(1), 1–5.

Padrón-Navarta, J. A., Sánchez-Vizcaíno, V. L., Hermann, J., Connolly, J. A. D., Garrido, C. J., Gómez-Pugnaire, M. T., & Marchesi, C. (2013). Tschermak's substitution in antigorite and consequences

for phase relations and water liberation in high-grade serpentinites. *Lithos*, *178*, 186–196. https://doi.org/10.1016/j.lithos.2013.02.001

Padrón-Navarta, J. A., Lopez Sánchez-Vizcaíno, V., Menzel, M. D., Gómez-Pugnaire, M. T., & Garrido, C. J. (2021). Mantle wedge oxidation due to sediment-infiltrated deserpentinisation. *Research Square*, PPR430498. https://doi.org/10.21203/rs.3.rs-1050656/v1

Pattison, D. R. M., & Newton, R. C. (1989). Reversed experimental calibration of the garnet-clinopyroxene Fe - Mg exchange thermometer. *Contributions to Mineralogy and Petrology*, *101*(1), 87–103. https://doi.org/10.1007/BF00387203

Piccoli, F., Hermann, J., Pettke, T., Connolly, J. A. D., Kempf, E. D., & Vieira Duarte, J. F. (2019). Subducting serpentinites release reduced, not oxidized, aqueous fluids. *Scientific Reports*, *9*(1), 19573. https://doi.org/10.1038/s41598-019-55944-8

Sack, R. O., & Ghiorso, M. S. (1991). Chromian spinels as petrogenetic indicators: thermodynamics and petrological applications. *American Mineralogist*, *76*(5–6), 827–847.

Savko, K. A., & Skryabin, V. Y. (1999). Petrology of forsterite-clinohumite marbles of the Voronezh Crystalline Massif. *Russian Geology and Geophysics*, *40*(4), 576–591.

Scambelluri, M., Bebout, G. E., Belmonte, D., Gilio, M., Campomenosi, N., Collins, N., & Crispini, L. (2016). Carbonation of subduction-zone serpentinite (high-pressure ophicarbonate; Ligurian Western Alps) and implications for the deep carbon cycling. *Earth and Planetary Science Letters*, *441*, 155–166. https://doi.org/10.1016/j.epsl.2016.02.034

Schneider, C. A., Rasband, W. S., & Eliceiri, K. W. (2012). NIH Image to ImageJ: 25 years of image analysis. *Nature Methods*, *9*(7), 671–675. https://doi.org/10.1038/nmeth.2089

Schwartz, S., Allemand, P., & Guillot, S. (2001). Numerical model of the effect of serpentinites on the exhumation of eclogitic rocks: Insights from the Monviso ophiolitic massif (Western Alps). *Tectonophysics*, *342*, 193–206. https://doi.org/10.1016/S0040-1951(01)00162-7

Schwartz, S., Guillot, S., Reynard, B., Lafay, R., Debret, B., Nicollet, C., et al. (2013). Pressure-temperature estimates of the lizardite/antigorite transition in high pressure serpentinites. *Lithos*, *178*, 197–210. https://doi.org/10.1016/j.lithos.2012.11.023

Schwarzenbach, E. M., Caddick, M. J., Beard, J. S., & Bodnar, R. J. (2016). Serpentinization, element transfer, and the progressive development of zoning in veins: evidence from a partially serpentinized harzburgite. *Contributions to Mineralogy and Petrology*, *171*(1), 5. https://doi.org/10.1007/s00410-015-1219-3

Sforna, M. C., Brunelli, D., Pisapia, C., Pasini, V., Malferrari, D., & Ménez, B. (2018). Abiotic formation of condensed carbonaceous matter in the hydrating oceanic crust. *Nature Communications*, *9*, 5049. https://doi.org/10.1038/s41467-018-07385-6

Shen, T., Hermann, J., Zhang, L., Lü, Z., Padrón-Navarta, J. A., Xia, B., & Bader, T. (2014). UHP metamorphism documented in Ti-chondrodite- and Ti-clinohumite-bearing serpentinized ultramafic rocks from Chinese southwestern Tianshan. *Journal of Petrology*, *56*(7), 1425–1458. https://doi.org/10.1093/petrology/egv042

Szlachta, V., Vlasov, K. & Keppler, H. (2022). On the stability of acetate in subduction zone fluids. Geochemical Perspective Letters, 21, 28-31. https://doi.org/10.7185/geochemlet.2213

Tao, R., Zhang, L., Tian, M., Zhu, J., Liu, X., Liu, J., et al. (2018). Formation of abiotic hydrocarbon from reduction of carbonate in subduction zones: Constraints from petrological observation and experimental simulation. *Geochimica et Cosmochimica Acta*, *239*, 390–408.

https://doi.org/10.1016/j.gca.2018.08.008

Toffolo L, Tumiati S, Villa A, Fumagalli P, Amalfa A and Miozzi F (2023), Experimental dissolution of carbonaceous materials in water at 1 GPa and 550°C: Assessing the role of carbon forms and redox state on COH fluid production and composition during forearc subduction of organic matter. *Frontiers in Earth Science,* 11:1013014. doi: 10.3389/feart.2023.1013014

Tumiati, S., & Malaspina, N. (2019). Redox processes and the role of carbon-bearing volatiles from the slab–mantle interface to the mantle wedge. *Journal of the Geological Society*, *176*(2), 388–397. https://doi.org/10.1144/jgs2018-046

Vandenbroucke, M., & Largeau, C. (2007). Kerogen origin, evolution and structure. *Organic Geochemistry*, *38*(5), 719–833. https://doi.org/10.1016/j.orggeochem.2007.01.001

Vieira Duarte, J. F., Piccoli, F., Pettke, T., & Hermann, J. (2021). Textural and Geochemical Evidence for Magnetite Production upon Antigorite Breakdown during Subduction. *Journal of Petrology*, *62*(10), egab053. https://doi.org/10.1093/petrology/egab053

Vitale Brovarone, A., Martinez, I., Elmaleh, A., Compagnoni, R., Chaduteau, C., Ferraris, C., & Esteve, I. (2017). Massive production of abiotic methane during subduction evidenced in metamorphosed ophicarbonates from the Italian Alps. *Nature Communications*, *8*, 14134. https://doi.org/10.1038/ncomms14134

8. Figures and captions

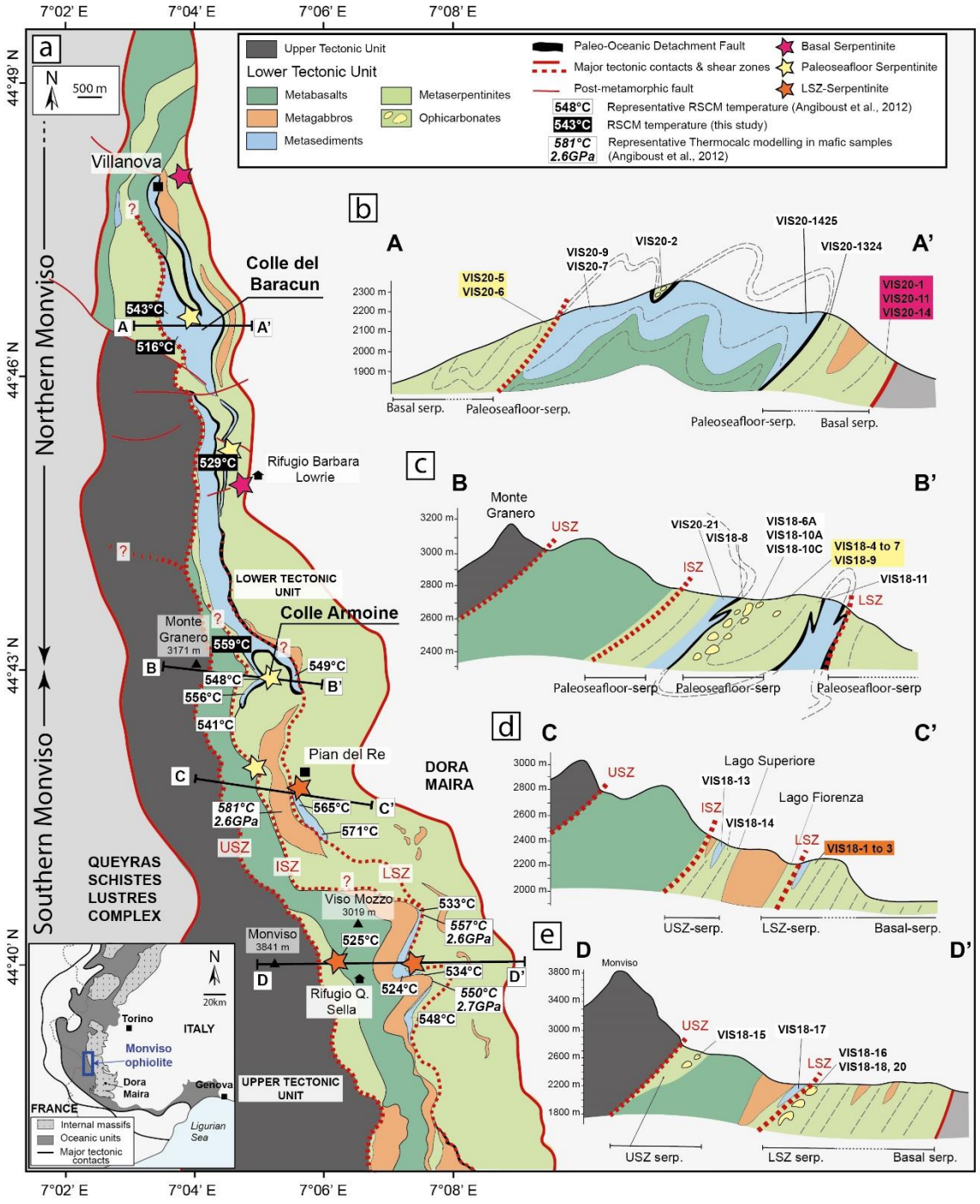

Figure 1. Geological map (a) of the Monviso meta-ophiolite and cross sections of Colle del Baracun (b; including a projection of sample locations spanning from Villanova, to the North, to Rifugio Barbara Lowrie further South), Colle Armoine (c), Lago Superiore and Lago Fiorenza (d) and Rifugio Quintino (Q.) Sella (e) areas (modified after (Angiboust et al., 2012; Balestro et al., 2018; Lombardo et al., 1978; Schwartz et al., 2001). The map at the bottom left shows the location of the Monviso meta-ophiolite

in the Western Alps (after Schwartz et al., 2001). (a) The Upper Shear Zone (USZ) (dashed red line extending from North to South) delimits the main tectonic unit of the Monviso meta-ophiolite, namely the Upper and Lower Tectonic Units (Angiboust et al., 2012). The solid dark line is interpreted by Balestro et al. (2015) as a paleo-Oceanic Detachment Fault (ODF) separating crustal and/or sedimentary lithologies from ultramafic units. Yellow and pinks stars correspond to serpentinites (serp.) sampled near and away the paleo-ODF (LSZ-serpentinites and basal serpentinites, respectively). Orange stars denote sampling within the USZ, the Lower Shear Zone (LSZ) and the Intermediate Shear Zone (ISZ). (b-e) Cross sections showing the sample locations along the eclogitic oceanic lithosphere of the Monviso massif. Sampling for. Representative P-T estimates derived from either RSCM in metasediments or Thermocalc modelling from Angiboust et al., 2012 and this study are reported in (a) (white and black boxes, respectively). Additional P-T estimates can be found in Angiboust et al. (2012), Blake et al. (1995) and Schwartz et al. (2001).

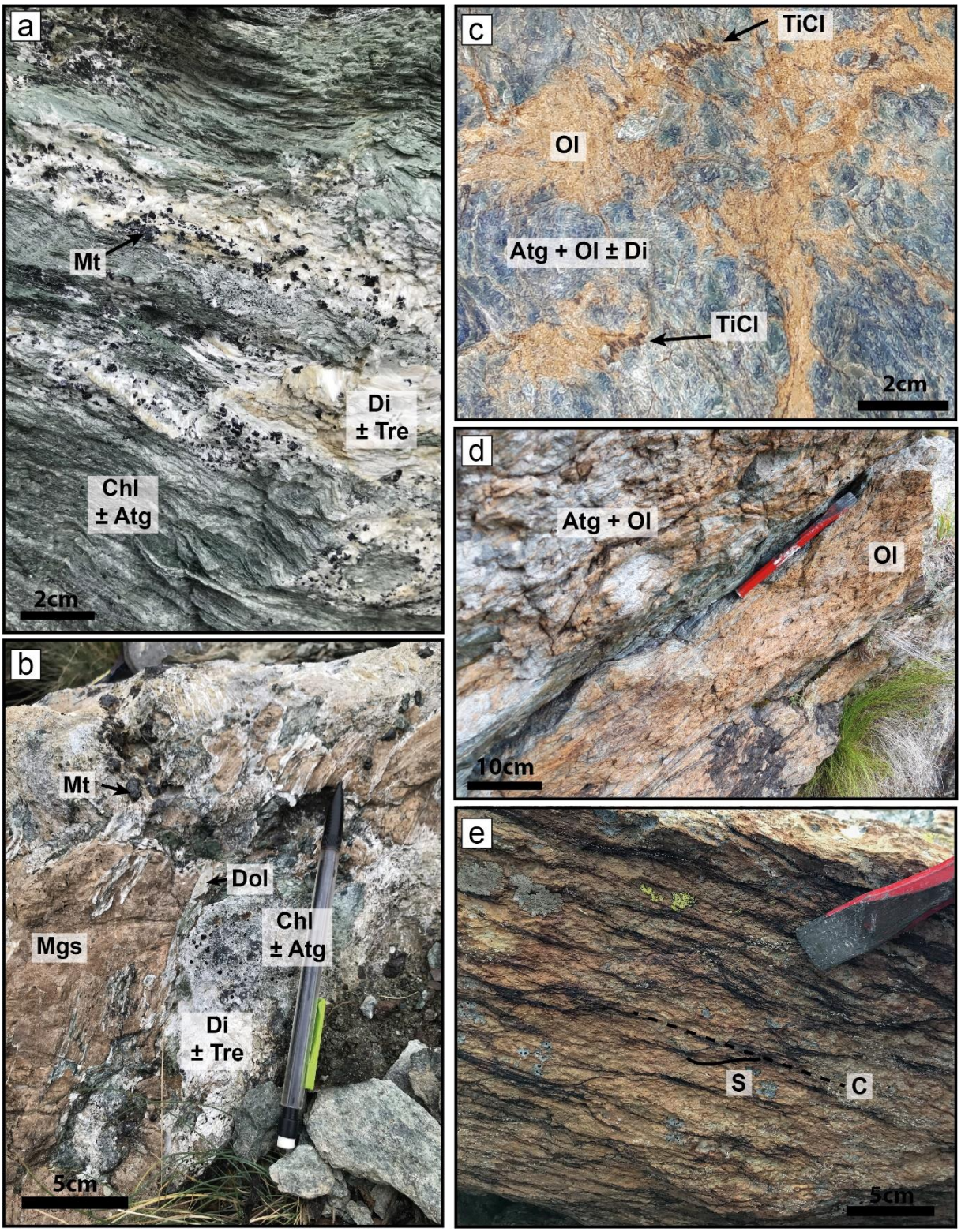

Figure 2. Field photographs of ultramafic rocks outcropping in the Monviso meta-ophiolite. (a) Chloriteschist made of an alternance of diopside-rich (± tremolite) and chlorite-rich (± antigorite) layers. Note that diopside is associated with abundant magnetite. (b) Meta-ophimagnesite embedded within chloriteschist foliation and displaying metamorphic coronas made of dolomite. (c) Olivine-

1037 bearing veins crosscutting paleoseafloor serpentinite. The veins are associated with humite crystals of
1038 centimetre size. (d) Basal serpentinite showing alternance of centimetre to metre sized brown olivine
1039 and serpentinite -rich layers. (e) LSZ-serpentinite where sigmoidal structures, underlined by brown
1040 olivine, contribute to a S-C fabric. See Table 1 caption for mineral abbreviations.

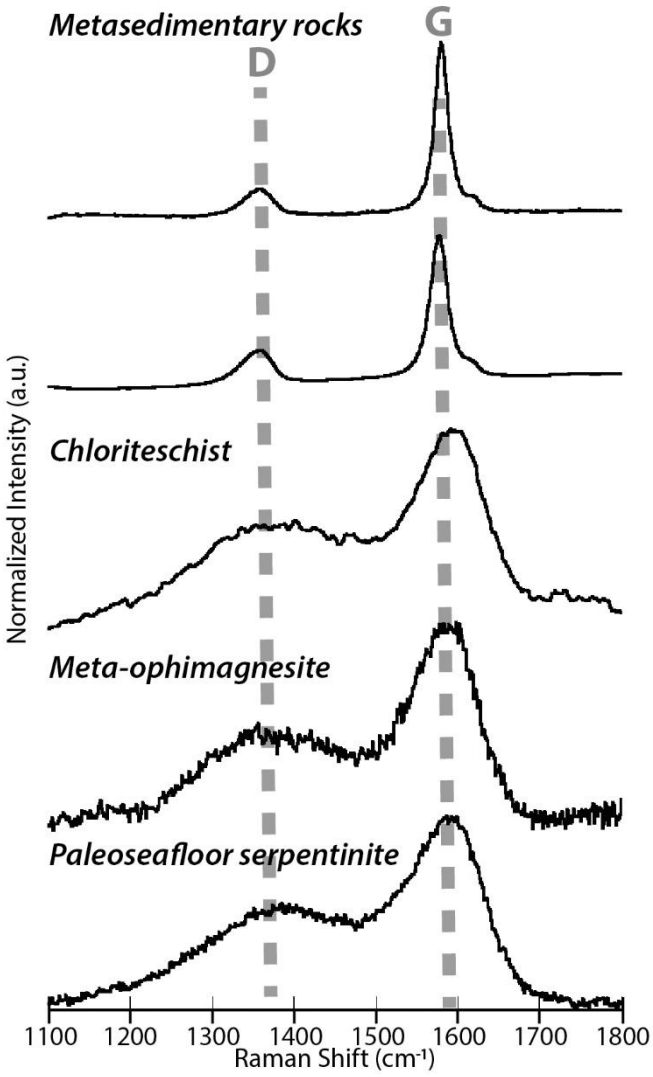

1041

1042 **Figure 3.** Raman spectra of organic matter composing metasedimentary rocks, chloriteschists, meta-
1043 ophimagnesites and paleoseafloor serpentinites. Note that the carbonaceous matter in ultramafic
1044 rocks is characterized by a broad and intense disordered band (D) and a large graphite band (G), while
1045 that in metasedimentary rocks is characterized by a sharp G band (G) of high intensity compared to
1046 the associated D band. a.u., arbitrary unit.

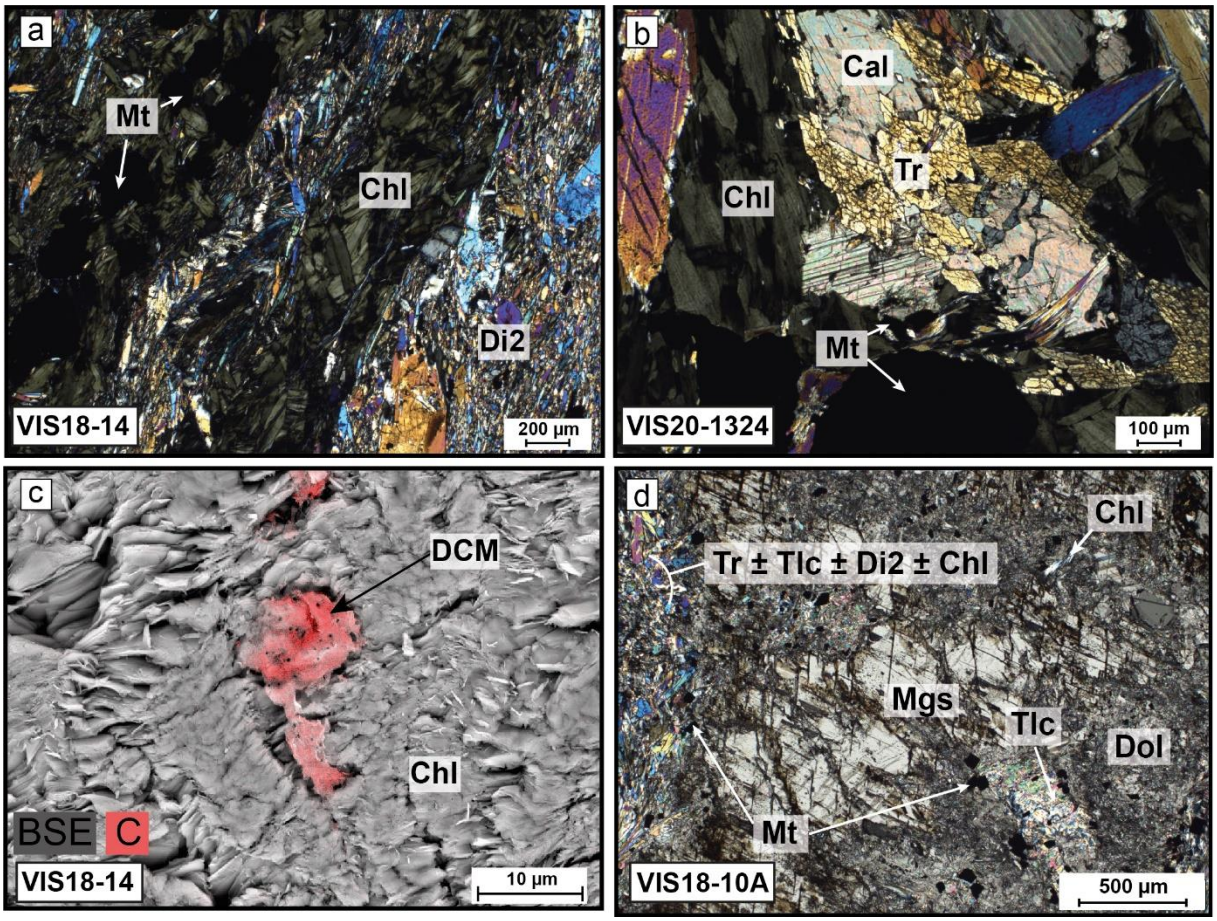

1047

1048 **Figure 4.** Petrological thin section (a,b) and hand-polished section (c,d) images of chloriteschists and
1049 meta-ophimagnesite from the Lago Superiore (a,c), the Rifugio Barbara Lowrie (b) and the Colle
1050 Armoine (b) . (a) Photomicrograph in crossed polarized light of a chloriteschist showing an alternance
1051 of metamorphic diopside (Di2)-rich and chlorite (Chl)-rich layers. Magnetite (Mt) is widely distributed
1052 in the sample. (b) Photomicrograph in crossed polarized light of a calcite (Cal) relict in chloriteschist.
1053 Calcite crystals present metamorphic corona made of tremolite and magnetite. (c) Overlay of SEM-BSE
1054 image and SEM-EDS image showing the distribution of carbon (in red), corresponding to DCM, within
1055 chlorite. (d) Photomicrograph in crossed polarized light of a meta-ophimagnesite. Magnesite (Mgs)
1056 metamorphic coronas are made from core to rims of dolomite (Dol), magnetite, talc (Tlc), tremolite
1057 (Tr), diopside and chlorite assemblages. Few lamellae of antigorite can also be observed within the
1058 metamorphic rims.

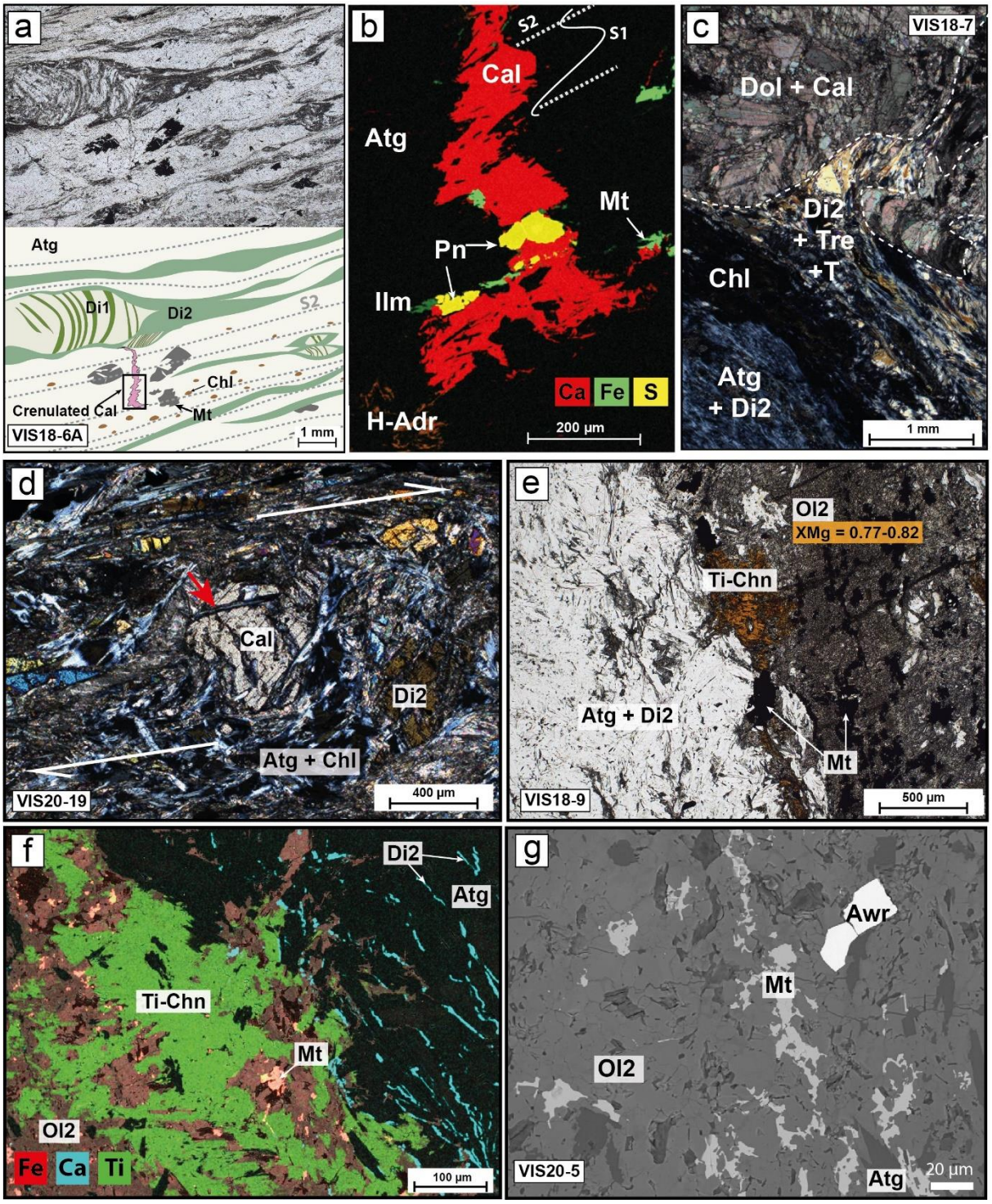

1059

1060 **Figure 5.** Photomicrographs of thin sections of paleoseafloor serpentinites from the Colle Armoine (a-
1061 f) and Colle del Baracun (g). (a) Photomicrograph in plane polarized light (top) and associated
1062 schematic illustration (bottom) of diopside bearing paleoseafloor serpentinites. The box indicates the
1063 location of the figure 7b. Metamorphic diopside(Di2)-rich layer, orientated along rock foliation (S2),
1064 embeds first generation of diopside (Di1) associated with antigorite (Atg). Magnetite (Mt) grains

display indented boundaries at the contact with antigorite. Elongated calcite (Cal) crystals of millimetre size are crenulated by the rock foliation. Chlorites (Chl) flakes can be observed in the centre of antigorite lamellae. (b) Composite SEM-EDS elemental image (with Ca in red, Fe in green, and S in yellow) of the elongated calcite shown in (a) and surrounded by a metamorphic rim made of pentlandite (Pn), hydro-andradite (H-Adr) and ilmenite (Ilm) in contact with antigorite. Calcite veins are orientated along an early S1 foliation and crenulated along rock S2 foliation. (c) Photomicrograph in crossed polarized light of a finely recrystallized carbonate porphyroclast made of dolomite (Dol) and calcite. The tail of the porphyroclast is made of tremolite (Tr), talc (Tlc) and metamorphic diopside. At the contact with the porphyroclast, the antigorite is fully recrystallized into chlorite. (d) Photomicrograph in crossed polarized light showing synthetic rotation (depicted by the white arrows) of a calcite porphyroclast. The metamorphic tail is made of metamorphic diopside, antigorite and chlorite. Note that calcite is overgrown by antigorite (red arrow). (e) Photomicrograph in plane polarized light of a partially dehydrated paleoseafloor serpentinite made of an alternance of metamorphic olivine- and antigorite-rich layers. Antigorite lamellae are associated with finely disseminated diopside (Di2) needles of 10 to 100 µm in length. Olivines (Ol2), whose XMg values (= Mg/(Mg + Fe)) are indicated, are associated with large crystals of titano-chondrodite (TiChn) and minute grains of magnetite (g). (f) Composite SEM-EDS image showing the distribution of iron (in red), calcium (in cyan) and titanium (in green) within antigorite- and olivine-rich layers. Antigorite layers are associated with finely disseminated calcium-rich needles corresponding to diopside (Di2). (g) Photomicrograph in reflected light of minute and interstitial grains of magnetite disseminated within olivine-rich layers.

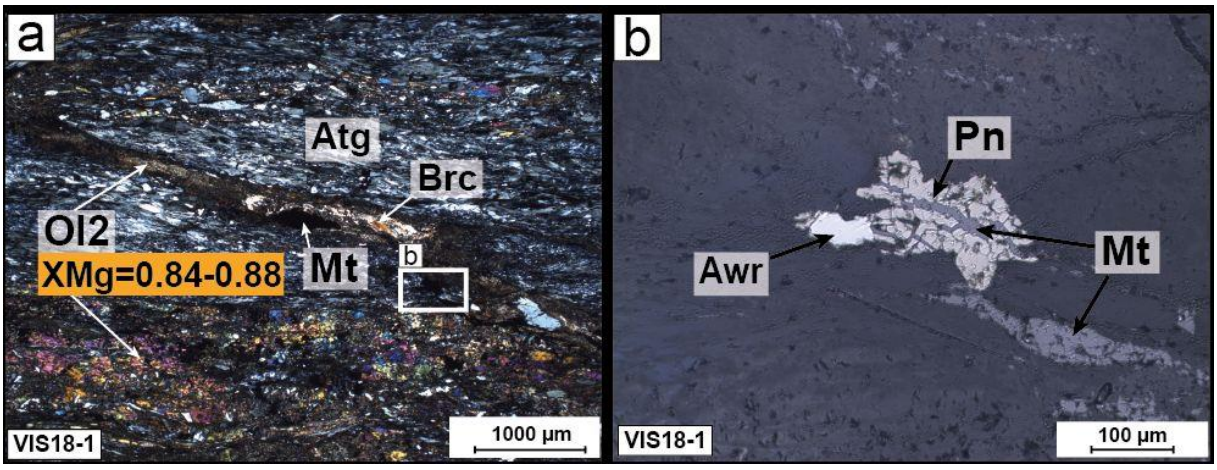

1087

1088 **Figure 6.** Thin section images of a LSZ-serpentinite sampled near the Lago Superiore. (a)
1089 Photomicrograph in crossed polarized light showing metamorphic olivine, brucite, antigorite and
1090 magnetite. Olivine-rich layers with associated range of XMg values are located at the contact between
1091 brucite and antigorite and define S-C structures (Figure 2e). (b) Photomicrograph in reflected light of
1092 magnetite-pentlandite-awaruite assemblage in olivine-rich layers (location shown in (a)). Note that
1093 pentlandite and awaruite surround a thin string of magnetite.

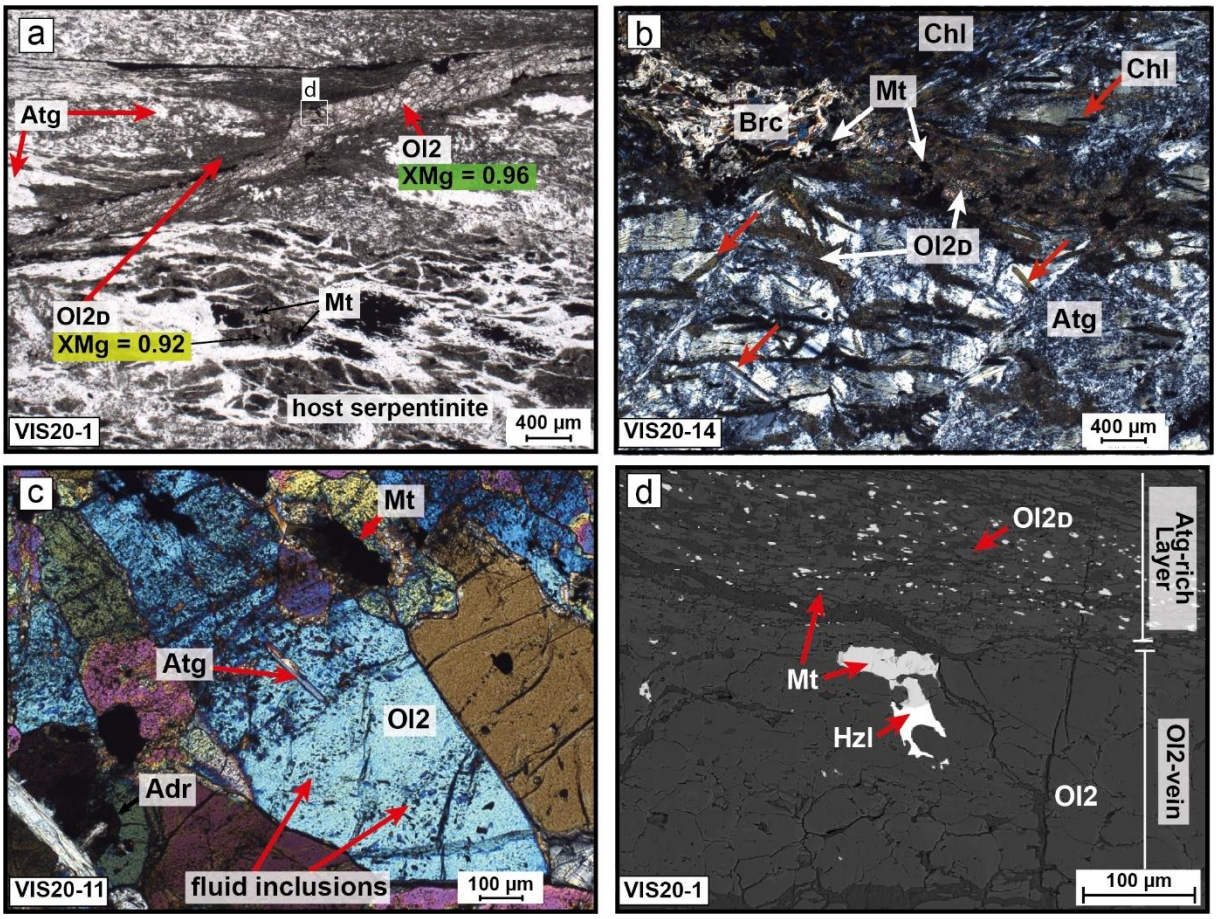

Figure 7. Thin sections images of basal serpentinites sampled at Villanova (a, d) and Rifugio Barbara Lowrie (b, c). (a) Photomicrograph in plane polarized light showing two generations of metamorphic olivines (dusty $Ol2_D$ and euhedral Ol2) and associated XMg values. The first generation is disseminated as large aggregates (>500 µm in width) within the host serpentinite. These aggregates are made of micrometric olivine grains associated with tiny magnetite (Mt) a few micrometres in width, giving a dusty texture in thin sections. The second generation is observed in veins made of euhedral olivines of a few hundreds of micrometres in width and that cross-cut the host serpentinite. The mean XMg value of the two olivine generations crystalizing in this sample are shown for comparison. (b) Photomicrograph in crossed polarized light showing pervasive dusty $Ol2_D$ vein network that surrounds hundreds of micrometres in width patches made of antigorite (Atg), chlorite (Chl), brucite (Brc) and/or magnetite. Flakes of antigorite can include chlorite in their centres (red arrows). (c) Photomicrograph in crossed polarized light of a massive Ol2-vein. Euhedral olivine crystals contain numerous fluid and mineral inclusions. These latter include antigorite, andradite (Adr), magnetite and heazlewoodite (Hzl).

1108 Secondary fluid inclusions are orientated along plans cross-cutting the olivine crystals. (d) SEM-BSE
1109 image of the contact between a large Ol2-vein and the host rock Ol1. Note that Ol2 are intimately
1110 associated with both magnetite and heazlewoodite.

1111

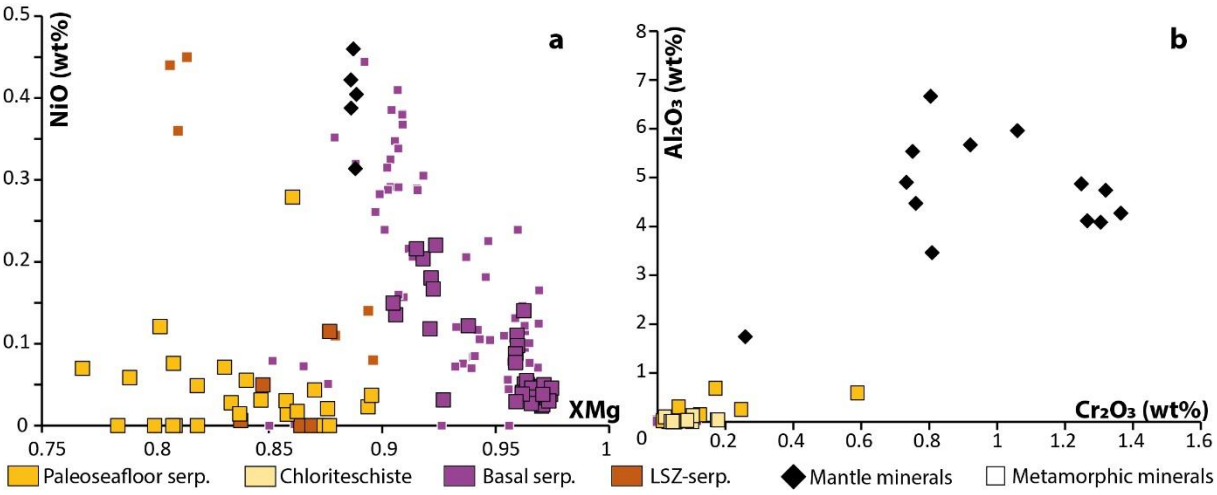

Figure 8. Chemical compositions in weight% (wt%) of (a) olivines and (b) diopsides from the Monviso metaserpentinites. Data from Schwartz et al. (2013) and Gilio et al. (2020) are shown for comparison (small symbols). (a) NiO content vs XMg value in olivines. Olivines of mantle origin have higher NiO contents than the ones of metamorphic origin. Paleoseafloor/LSZ- and basal serpentinites have, respectively, lower and higher XMg values than the olivines of mantle origin. (b) Al_2O_3 vs Cr_2O_3 in diopsides. Metamorphic diopsides (Di2) have lower Al_2O_3 and Cr_2O_3 contents than the primary ones (Di1). Uncertainties fall within symbol sizes.

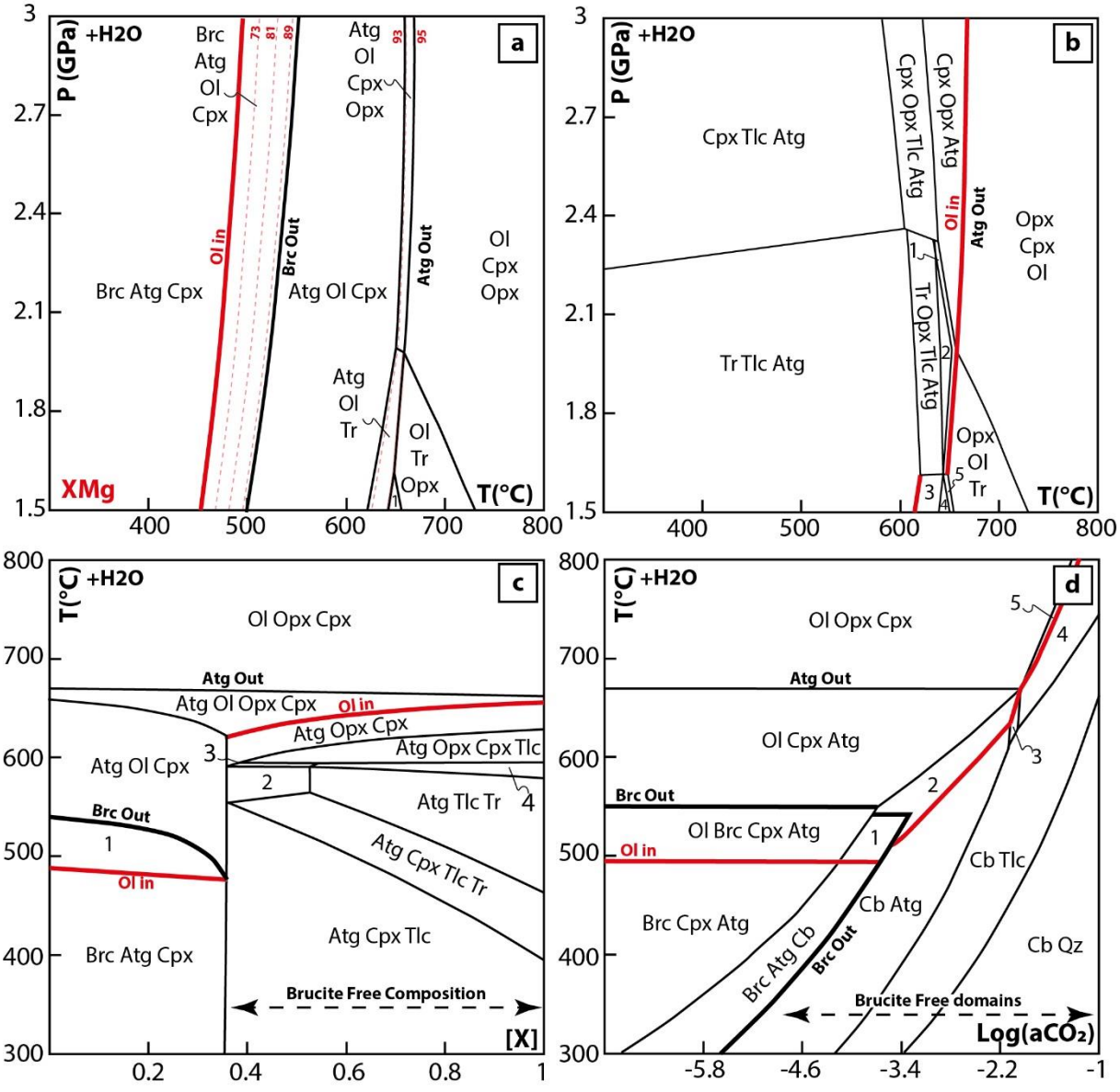

Figure 9. Pseudosections based on bulk rock compositions of (a, c, d) olivine-rich (sample VIS18-5A1) and (b) diopside-rich (sample VIS18-7) paleoseafloor serpentinites. (a-b) P-T pseudosections showing two metamorphic sequences in paleoseafloor serpentinites influencing the appearance of olivine (Ol in). (c) T-X pseudosection at 2.5 GPa using MgO variations observed in paleoseafloor serpentinites (from 36.95 at [X] = 0, to 25.88 wt% at [X] = 1). MgO-rich systems are characterized by a paragenesis made of Atg-Ol-Cpx at metamorphic climax (520-570°C-2.6-2.7 GPa) while in SiO_2-rich systems, the olivine appearance is push back to >620°C. (d) T-Log(aCO_2) pseudosection at 2.5 GPa and a water activity of 1 in order to report on aCO_2 effects only. The increase of CO_2 activity reduces the divariant field of brucite, pushing up the appearance of olivine to higher temperatures. Atg, antigorite; Brc,

brucite; Cpx, clinopyroxene; Ol, olivine; Opx, orthopyroxene; Q, quartz; Tlc, talc; Tr, tremolite; Cb stands for carbonates. (a), 1: Ol-Tlc-Tr; (b), 1: Opx-Cpx-Atg-Tr; 2: Opx-Atg-Tr; 3: Ol- Atg-Tlc-Tr; 4: Ol-Tlc-Tr; (c), 1: Ol-Brc-Cpx-Atg; 2: Cpx-Atg-Tr; 3: Opx-Tr-Cpx-Atg; 4: Tr-Tlc-Atg-Opx; (d) 1: Ol-Brc-Cb-Atg; 2: Ol-Cb-Atg; 3: Opx-Cb-Atg; 4: Opx-Cb; 5: Opx-Ol-Cb.

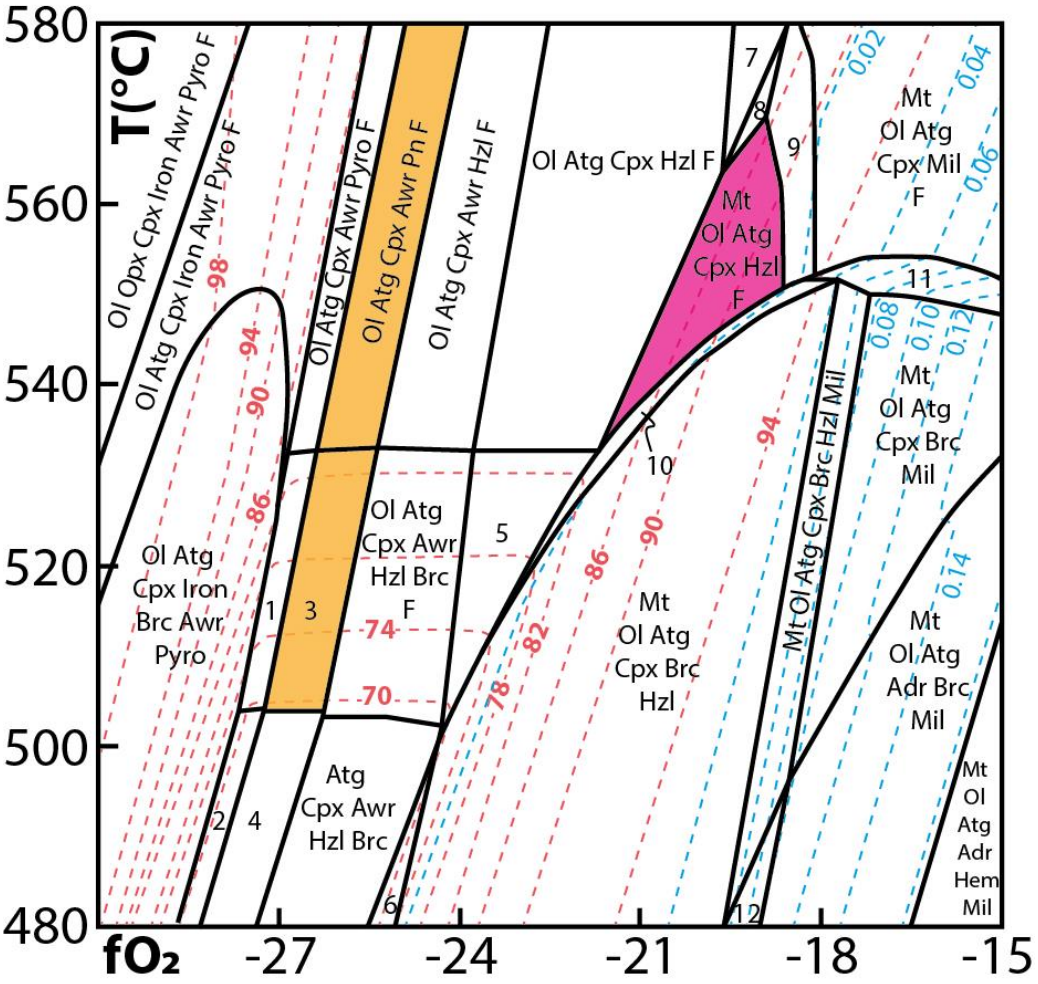

1135

1136 **Figure 10.** T-Log(fO_2) pseudosection at 2.5 GPa in the S-NiO-CaO-FeO-MgO-SiO_2-H_2O system using
1137 VIS18-5A1 sample composition. XMg value and NiO content (wt%) isopleths of olivine are in dashed
1138 red and blue, respectively. Conditions of formation of basal versus ODF-serpentinites (and LSZ-
1139 serpentinites) are shown in pink and orange, respectively. Atg, antigorite; Adr, andradite; Awr,
1140 awaruite; Brc, brucite; Chl, chlorite; Cpx, clinopyroxene; Hem, hematite; Hzl, heazlewoodite; Iron,
1141 native iron; Mil, millerite; Mt, magnetite; Ol, olivine; Opx, orthopyroxene; Pn, pentlandite; Pyro,
1142 pyrrhotite; suffix F stands for fluids. 1: Ol-Brc-Atg-Cpx-Awr-Pyro-F; 2: Brc-Atg-Cpx-Awr-Pyro; 3: Ol-Brc-
1143 Atg-Cpx-Awr-Pn-F; 4: Brc-Atg-Cpx-Awr-Pn; 5: Ol-Brc-Atg-Cpx-Hzl-F; 6: Atg-Brc-Ol-Cpx-Mt-Awr-Hzl; 7:
1144 Atg-Ol-Cpx-Hzl-Pn-F; 8: Atg-Ol-Cpx-Hzl-Pn-Mgt-F; 9: Atg-Ol-Cpx-Hzl-Mil-Mgt-F; 10: Atg-Brc-Ol-Cpx-Brc-
1145 Mt-Hzl-Mil-F; 11: Ol-Brc-Atg-Cpx-Mt-Mil-F; 12: Ol-Brc-Atg-Mt-Adr-Hzl-Mil.

1146

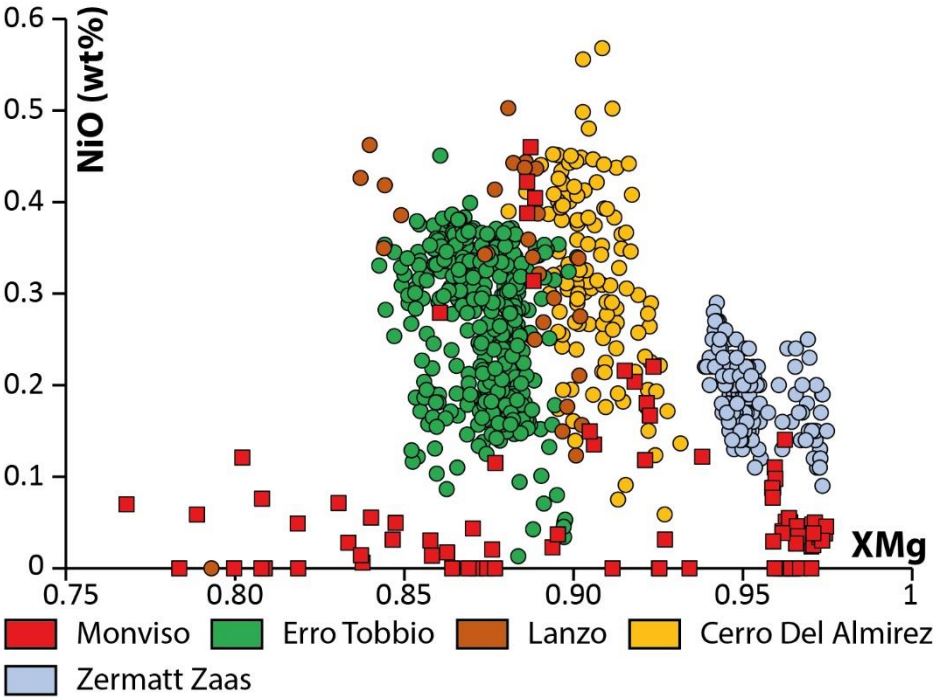

Figure 11: NiO content vs XMg value in metaserpentinite olivines from different alpine eclogitized meta-ophiolite massifs. Data from are from this study and Gilio et al. (2020) for the Monviso, Peters et al. (2020) for Erro Tobbio, Debret et al. (2013) for the Lanzo, Bretscher et al. (2020) for Cerro del Almirez and Kempf et al. (2020) for Zermatt Zaas.